

**NON-THERMAL INTERACTIONS ON LOW  
TEMPERATURE ICE AND AQUEOUS INTERFACES**

A Dissertation  
Presented to  
The Academic Faculty

by

Janine Elizabeth Captain

In Partial Fulfillment  
of the Requirements for the Degree  
Doctor of Philosophy in Chemistry

Georgia Institute of Technology

May 2005

# **NON-THERMAL INTERACTIONS ON LOW TEMPERATURE ICE AND AQUEOUS INTERFACES**

Approved by:

Dr. Thomas Orlando, Advisor  
School of Chemistry and Biochemistry  
*Georgia Institute of Technology*

Dr. Paul Wine  
School of Chemistry and Biochemistry  
*Georgia Institute of Technology*

Dr. Boris Mizaikoff  
School of Chemistry and Biochemistry  
*Georgia Institute of Technology*

Dr. Jiri Janata  
School of Chemistry and Biochemistry  
*Georgia Institute of Technology*

Dr. Greg Huey  
School of Earth and Atmospheric Sciences  
*Georgia Institute of Technology*

Date Approved: April 1, 2005

## **ACKNOWLEDGEMENT**

These past five years have been filled with many opportunities as well as challenges, and I have been fortunate to have the support that allowed me to develop as both a scientist and an individual. My advisor, Dr. Thomas Orlando, gave me the opportunity to learn new techniques to address scientific issues which were of interest to me. Although we didn't always agree on things, he was always supportive of my scientific direction and has prepared me for the challenges I will face in my scientific career. Dr. Alexandr Aleksandrov provided his knowledge from previous experiences when discussing and interpreting much of the data. His disbelief and unique viewpoints challenged me to prove my point and has taught me to be a better scientist. Dr. Gregory Grieves offered a fresh perspective in the last two years and has provided leadership as well as contributed his knowledge to the group.

I would like to thank my husband Jim, who has taught me that things aren't as hard as they may seem, and for all of his love and encouragement. His strength has allowed me to reach new heights. My parents taught me the foundations of hard work and responsibility that carried me through all these years of school. The care packages and phone calls were wonderful reminders of the love and support of my family. I would also like to thank my friends who have made this journey more enjoyable, taught me things that I could never learn in school, and gave me memories that will last a lifetime.

## TABLE OF CONTENTS

ACKNOWLEDGEMENTS	iii
LIST OF FIGURES	vii
LIST OF SYMBOLS AND ABBREVIATIONS	ix
SUMMARY	xii
CHAPTER 1 INTRODUCTION	1
1.1 Background	1
1.2 Utility of Electron Stimulated Desorption (ESD) and Photon Stimulated Desorption (PSD)	5
CHAPTER 2 UHV ENVIRONMENTAL CHAMBER	8
2.1 Overview	8
2.2 Sample	9
2.3 Time-of-Flight (TOF) Mass Spectrometer	10
2.4 Electron Gun	11
2.5 Pulsing Sequence	11
2.6 Quadrupole Mass Spectrometer (QMS)	12
2.7 Dosing System	13
CHAPTER 3 ESD OF CATIONS FROM PRISTINE ICE SURFACES	16
3.1 Overview	16
3.2 Experimental Details	17
3.3 Results	19

3.3.1 Time-of-Flight (TOF) Spectra	19
3.3.2 Cation ESD Threshold Energies	21
3.3.3 Kinetic Energy Distributions	22
3.3.4 Temperature Dependent Yields	27
3.4 Discussion	28
3.4.1 Electronic Structure of Ice	28
3.4.2 Mechanism of $H^+$ Desorption	32
3.4.3 Mechanism of $H_2^+$ Desorption	34
3.4.4 Mechanism of Cluster Ion Desorption	36
3.4.5 Cluster Growth and Ejection	38
3.4.6 Temperature Effects	42
CHAPTER 4 INTERACTION OF HCl WITH ICE SURFACES	46
4.1 Overview	46
4.2 Experimental Details	47
4.3 Time-of-Flight (TOF) Spectra of HCl Dosed Ice Surfaces	49
4.4 Cation Yield as a Function of HCl Coverage	51
4.5 Isotope Exchange	53
4.6 Velocity Distribution of Protons With and Without Adsorbed HCl	56
4.7 Temperature Programmed Desorption (TPD) of HCl: Ice at Several Growth Temperatures	58
4.8 Cation ESD Mechanism	61
4.8.1 Proton Desorption Mechanism	61
4.8.2 $H_2^+$ Desorption Mechanism	63
4.8.3 Cluster Desorption Mechanism	64
4.9 Mechanism of HCl Effects on Cation ESD	65
4.10 Temperature Programmed Desorption (TPD) Discussion	67
CHAPTER 5 LIQUID JET CHAMBER DESCRIPTION	70
5.1 Motivation for Liquid Jet Chamber	70

5.2 Previous Work on Liquid Jets	71
5.3 Experimental Setup	73
5.3.1 Liquid Jet	73
5.3.2 Excimer Laser	75
5.3.3 Time-of-Flight (TOF) Mass Spectrometer	76
5.3.4 Salt Solutions	76
CHAPTER 6 PSD OF SODIUM SALT SOLUTIONS IN LIQUID JET	78
6.1 Overview	78
6.2 Time-of-Flight (TOF) Spectra	79
6.3 Concentration Dependence of Cation Yield	79
6.4 Anion Dependence of Cation Yield	82
6.5 Flux Dependence of Cation Yield	84
6.6 Collision Free Desorption	85
6.7 Evaporation from the Jet Surface	86
6.8 Mechanism and Model of Cation Desorption from the Liquid Jet Surface	87
6.9 Analysis of Photon Flux Dependence	92
CHAPTER 7 CONCLUSIONS	94
7.1 Relevant Atmospheric Chemistry Studies	94
7.2 Implications of this Work to Atmospheric Chemistry	99
7.3 Continuation of Research	101
7.4 Conclusion	102
7.4.1 ESD of Pristine Ice Surfaces	102
7.4.2 Probing the Interaction of HCl with Ice Surfaces	103
7.4.3 Photoionization of Sodium Salt Solutions in a Liquid Jet	104
REFERENCES	105

## LIST OF FIGURES

Figure 2.1	Schematic of UHV environmental surface science chamber	8
Figure 3.1	ESD-TOF from ~ 50 ML of CI, ASW, and PASW	20
Figure 3.2	ESD threshold measurements of $\text{H}_2^+$ and water clusters ( $\text{H}^+(\text{H}_2\text{O})_{n=1-3}$ )	23
Figure 3.3	Proton kinetic energy distributions from CI and PASW	24
Figure 3.4	Measured and calculated kinetic energy distributions of proton and cluster ions from PASW	26
Figure 3.5	Temperature dependence of ESD cation yields from ice, inset shows temperature programmed desorption of water	28
Figure 3.6	Molecular orbital diagram of water	29
Figure 3.7	Photoemission spectra of ASW and CI	30
Figure 3.8	Two-hole and two-hole one-electron configurations of water	33
Figure 3.9	Model fit to cluster distribution	40
Figure 3.10	Coulomb repulsion between two point charges	41
Figure 3.11	Temperature dependence of Debye-Huckel screening distance	45
Figure 4.1	Cation yield of pristine and HCl dosed ice surfaces	50
Figure 4.2	Cation yield as a function of HCl coverage	52
Figure 4.3	Isotope exchange in dimer cluster	55
Figure 4.4	Velocity distributions of protons with and without adsorbed HCl	57
Figure 4.5	TPD of HCl dosed ice from CI, ASW, and PASW	60
Figure 5.1	Schematic of liquid jet	74

Figure 6.1	TOF spectra of sodium salt solutions of concentrations from $10^{-4}$ – $10^{-1}$ M	80
Figure 6.2	Concentration dependence of cluster yield from NaCl, NaBr, and NaI	81
Figure 6.3	TOF spectra of $10^{-1}$ M NaBr solution	83
Figure 6.4	TOF spectra of $10^{-1}$ M NaI solution	84
Figure 6.5	Power dependence of cation yield from a $10^{-2}$ M NaI solution	85
Figure 6.6	Model fit of cluster distribution from NaCl solutions	90
Figure 6.7	Model fit of cluster distribution from NaBr solutions	91



## LIST OF SYMBOLS AND ABBREVIATIONS

$1/\tau$	critical lifetime
Å	Angstrom
amu	Atomic Mass Units
API-MS	Atmospheric Pressure Ionization Mass Spectrometry
ASW	Amorphous Solid Water
ATR	Attenuated Total Reflection
CI	Crystalline ice
DC	direct current
$E_a$	Activation Energy
EA	Electron Affinity
$E_H$	Energy of a hydrogen bond (0.25 eV)
$E_n, E_m$	Energy of a solvated ion with n, m water molecules ( $H^+ - n, Na^+ - m$ )
ESD	Electron Stimulated Desorption
eV	Electron Volts
fs	Femtosecond
FT-IR	Fourier Transform Infrared Spectroscopy
g	Grams
HPLC	High Performance Liquid Chromatography
Hz	Hertz
I	Intensity
ICD	Intermolecular Coulomb Decay

IP	Ionization Potential
K	Kelvin
kJ	Kilojoules
L	length
<i>m</i>	Mass
M	Molar
m	number of water molecules in solvated sodium ion cluster
MAGIC	Model of Aerosol, Gas and Interfacial Chemistry
MCS	Multi-Channel Scalar
min	Minutes
mJ	MilliJoules
ml	Milliliter
ML	Monolayer
mol	Mole
MPa	MegaPascal
n	number of water molecules in protonated water cluster
NAT	Nitric Acid Trihydrate
NEXAFS	Near Edge X-ray Absorption Fine Structure spectroscopy
nm	Nanometer
nsec	Nanosecond
pA	Picoamps
PASW	Porous Amorphous Solid Water
PSC	Polar Stratospheric Cloud

PSD	Photon Stimulated Desorption
QM/MM	Quantum Mechanical / Molecular Mechanics
QMS	Quadrupole Mass Spectrometer
QMS	Quadrupole Mass Spectrometer
RF	radio frequency
RIS	Reactive Ion Scattering
sec	Second
SIMS TOF	Secondary Ion Mass Spectrometry Time of Flight
t	Time
TOF	Time of Flight
TPD	Temperature Programmed Desorption
$U_e$	Effective hole-hole interaction
UHV	Ultra-High Vacuum
UV	Ultraviolet
V	Volts
XES	X-ray Emission Spectroscopy
$\Gamma$	bandwidth (photoemission spectroscopy)
$\mu\text{m}$	Microns

## SUMMARY

Electron-impact ionization of low-temperature water ice leads to  $H^+$ ,  $H_2^+$ , and  $H^+(H_2O)_{n=1-8}$  desorption. The threshold energy for ESD of  $H_2^+$  from CI and  $H_3O^+$  from PASW and ASW is  $\sim 22 \pm 3$  eV. There is also a  $H_2^+$  yield increase at  $\sim 40 \pm 3$  eV and a  $\sim 70 \pm 3$  eV threshold for ESD of  $H^+(H_2O)_{n=2-8}$  from PASW and ASW.  $H_2^+$  production and desorption involves direct molecular elimination and reactive scattering of an energetic proton. Both of these channels likely involve localized two-hole one-electron and/or two-hole final states containing  $4a_1$ ,  $3a_1$  and/or  $2a_1$  character. The 70 eV cluster ion threshold implicates either an initial ( $2a_1^{-2}$ ) state localized on a monomer or the presence of at least two neighboring water molecules each containing a single hole. The resulting correlated two-hole or two-hole, one-electron configurations are localized within a complex and result in an intermolecular Coulomb repulsion and cluster ion ejection.

The changes in the yields with phase and temperature are associated with structural and physical changes in the adsorbed water and longer lifetimes of excited state configurations containing  $a_1$  character. The dependence of the ESD cation yields on the local potential has been utilized to examine the details of HCl interactions on low temperature ice surfaces. The addition of HCl increases cluster ion yields from pure ice while decreasing  $H^+$  and  $H_2^+$  yields. These changes reflect the changes in the local electronic potential due to the changing bond lengths at the surface of the ice as HCl ionizes and the surrounding water molecules reorient to solvate the ions.

This work has been extended to ionic solutions at higher temperatures using a liquid jet and ultraviolet photoionization to interrogate the surface of aqueous ionic interfaces. Desorption of protonated water clusters and solvated sodium ion clusters were measured over a range of concentrations from NaCl, NaBr, and NaI solutions. The flux dependence indicated a multiple photon process and the proposed mechanism involves a Coulomb explosion resulting from the repulsion of nearby ions. The surface is investigated with regard to its importance in heterogeneous atmospheric chemistry.

# CHAPTER 1

## INTRODUCTION

### 1.1 Background

Ice is a ubiquitous molecular solid and its properties (i.e. the electronic structure, hydrogen bonding network, electrical conductivity and dynamics) have been the subject of numerous investigations. Understanding these properties, particularly at low temperature ( $< 200$  K), is very important in atmospheric physics and chemistry<sup>1-4</sup>, astrophysics<sup>5</sup>, geophysical and planetary sciences<sup>6</sup>. Due the structural similarities of low temperature ice surfaces with water in the liquid state<sup>7</sup>, the study of nanoscale ice films and interfaces may also have direct relevance to the study of biological systems. Thus, the interaction of radiation with low temperature ice has also been studied extensively since it is relevant to radiation treatment and damage of biological material<sup>8,9</sup>.

Heterogeneous processes play an important role in the chemistry occurring in the atmospheric polar regions since many reactions are relatively slow or forbidden in the gas phase<sup>2</sup>. Surface interactions can lower the activation energy barriers for reactions that would normally not occur in the gas phase. Some of the most well studied heterogeneous interactions involve polar stratospheric cloud (PSC) particles. These PSCs provide a water/ice surface for reactions involving halogens and acids<sup>10</sup>. For example, the reactions  $\text{HCl} + \text{ClONO}_2 \rightarrow \text{Cl}_2 + \text{HNO}_3$  and  $\text{HCl} + \text{HOCl} \rightarrow \text{Cl}_2 + \text{H}_2\text{O}$  are thought to occur on PSCs. The  $\text{Cl}_2(\text{g})$  can photodissociate to form Cl atoms<sup>2, 4, 11</sup> which then react irreversibly with ozone. Since understanding heterogeneous reactions on PSCs will help

improve current atmospheric models, determining the dynamics and details of surface and interface reactions on PSCs is critical. An important initial step is to determine whether the reactants are present in ionized or solvated forms versus chemisorbed molecular states.

The air/water interface is a dynamic environment that is not well understood. The water molecules at the surface have fewer hydrogen bonds and increased diffusion compared to the bulk molecules, yet they do not behave like gas-phase molecules. It is the behavior and reactivity of these terminal water molecules that is not well understood and difficult to investigate. Recent simulations by Jungwirth and Tobias<sup>12-16</sup> on the structure of the air/water interface of aqueous salt solutions provide evidence of the presence of anions on the surface, in contrast to the conventional belief of an ion-free interface.

Recent experimental and theoretical work examining the photochemical reactions of aqueous NaCl aerosols<sup>16</sup> has led to the conclusion that reactions occurring at the air/water interface must be dominant to reproduce experimental data with kinetic modeling. Many of the experimental investigations into photochemical reactions employ bulk techniques that measure the products of a system. While this provides some information regarding the overall reaction, it cannot determine the mechanisms involved in the reactions. The kinetic models require a step-by-step reaction scheme with accurate rate constants. The state of the surface species is important because reactions involving hydrated ions are very different than reactions involving molecular species. The region in which a reaction occurs also affects the overall rate at which it occurs. If a reaction were to occur at the interface instead of in bulk solution, the overall rate could

dramatically change. The reactants would no longer need to diffuse into the bulk and meet in solution, but gaseous species could react with species at the interface.

Low temperature ice surfaces provide a dynamic system that will give insight into reactions on PSCs. Ice surfaces at higher temperatures are complicated by rapid desorption and adsorption, with evaporation rates on the order of  $10^{16}$ - $10^{18}$  molecules/s  $\text{cm}^2$  between 180-210 K<sup>17</sup>. The surface of the ice at these temperatures is constantly changing and the structure and dynamic response of the terminal water layer is difficult to describe. Lower temperatures and ultra-high vacuum (UHV) conditions will decrease the evaporation rates and allow us to obtain a basic understanding of how molecules interact with ice, albeit at temperatures lower than those which are typical of the stratosphere.

Specifically, the interaction of HCl with ice surfaces is of importance in understanding a simple ionization reaction at this complex air/solution interface. Several studies have investigated the interaction of adsorbates such as HCl on low temperature ices under high or ultra-high vacuum conditions. Kang et al. used reactive ion scattering (RIS) and low energy secondary ion mass spectrometry (SIMS) to measure the extent of ionization with temperature and found mostly molecular HCl at temperatures below 70 K<sup>18</sup>, a mixture of the ionized and molecular forms of HCl from 90-120 K, and complete ionization above 140 K. This technique, however, when not used with grazing incident ions, can affect the surface when probing it through momentum transfer from the incoming ion. The probe may actually induce ionization at temperatures lower than temperatures at which ionization occurs naturally or spontaneously. Molecular beam experiments<sup>19</sup> have found two types of HCl adsorption at temperatures between 100-170 K, assigned as molecular HCl adsorption and a second ionized or hydrated species. HCl



has been shown to aid in further dissolution of HCl molecules, with the  $\text{Cl}^-$  ion acting to solvate the hydrogen side of the incoming HCl molecule<sup>20</sup>. Thus, high concentrations of HCl may skew the observed ionization temperature, because these higher doses might not reflect HCl- $\text{H}_2\text{O}$  interactions, but HCl- $\text{Cl}^-$  interactions. In addition, spectroscopic studies have shown evidence of complete ionization at 80 K<sup>21, 22</sup> on ice films, while others report molecular bands that exist up to 125 K<sup>23</sup>. Near-edge X-ray absorption fine structures (NEXAFS) has been used with photo-stimulated desorption NEXAFS to probe the interaction of HCl and ice in the bulk and on the surface<sup>24</sup>, respectively. These measurements provide evidence of ionization both in the bulk and at the surface; the molecular HCl signal is not present when 1 L of HCl is adsorbed on 100 L of crystalline ice at 120 K and changes due to the solvated  $\text{Cl}^-$  ion appear in the spectra.

The temperature programmed desorption (TPD) of HCl on ice is complicated by many factors that can be varied such as growth temperature of the ice, annealing history of the ice, and the temperature at which HCl is dosed. There are several experimental studies of HCl desorption from ice<sup>25-28</sup>. It is generally agreed upon that the ionized or hexahydrate HCl species desorbs between 150 - 160 K, however, there are differences in the interpretation of the lower temperature features that will be discussed in Chapter 4.

Several theoretical and modeling studies have attempted to describe solvation at ice surfaces. Gertner and Hynes<sup>29</sup> employed molecular dynamics simulations of HCl on the surface of ice at 190 K and suggested that the HCl was initially incorporated as a molecular species into the ice lattice (not the bulk). In this case, there was a barrier for dissociation since the dynamic lattice response was not taken into account. However,

more recent studies by Bolton et. al.<sup>30</sup> and Buch et. al.<sup>20</sup> clearly demonstrated the importance of defect configurations and the dynamic lattice relaxation of the ice.

## **1.2 Utility of Electron Stimulated Desorption (ESD) and Photon Stimulated Desorption (PSD)**

The interaction of electrons with molecular solids such as ice is a topic of wide concern in many fields such as astrophysics, materials physics, atmospheric physics, biophysics, planetary and environmental science. Of particular interest is the interaction of low-energy electrons with condensed water since this is important in i) radiation processing of outer solar system grains and bodies<sup>6</sup>, ii) radiation damage of biological targets<sup>31</sup>, iii) formation of planetary atmospheres<sup>5</sup> and iv) stimulating heterogeneous reactions possibly involved in loss of atmospheric ozone<sup>1-4</sup>.

Electron stimulated desorption (ESD) is an extremely sensitive surface specific probe that has been used to study the near-surface structure of ice<sup>6, 32, 33</sup>. The two features that make ESD inherently surface sensitive are (1) the electrons have a low penetration depth and (2) the desorbing cation species must be produced at the surface or near surface to desorb from the bulk sample. It has been shown that the ESD products can be greatly affected by small changes in the local potential and excited state lifetimes of the surface molecules<sup>32</sup>. Using ESD, we can examine the temperature and phase dependence of the cation yields to gain insight into the dynamic interactions of small molecules with low-temperature ice surfaces.

The ESD of energetic and thermalized neutral particles from ice can be explained in terms surface and self-trapped low-energy ( $E < E_g$ ) excitons decay<sup>34</sup>. These excitons

are also the parent states for one-hole, two-electron Feshbach resonances which decay to yield primarily  $\text{H}^{-35, 36}$  and  $\text{O}^{-35}$ . Due to the very local nature of the electron scattering resonances,  $\text{H}^-$  yields are dependent upon ice temperature and phase and  $\text{O}^-$  yields are reduced due to the polarization interaction and lattice response.

The production and release of positively charged products from ice requires much more energy and is dominated by the desorption of protons with essentially no observable higher mass ions<sup>32, 37</sup>. This is largely due to efficient hole-hopping and delocalization brought about by the hydrogen bonding network<sup>32, 37</sup> and the lattice response to local charges. In general, hole-localization probabilities and desorption of  $\text{H}^+$ ,  $\text{H}_2^+$ , and  $\text{H}^+(\text{H}_2\text{O})_{n=1-8}$  should be very dependent upon the local hydrogen bonding network. Thus, ESD of  $\text{H}^+$ ,  $\text{H}_2^+$ , and  $\text{H}^+(\text{H}_2\text{O})_{n=1-8}$  should be sensitive probes of the terminal ice structure and the dynamical interactions on ice surfaces.

High-energy radiation, such as cosmic rays, x-rays or gamma-rays, have relatively large penetration depths and primarily probe bulk processes. These particles lose energy in condensed-phase media via ionization producing large numbers of secondary electrons that must undergo inelastic scattering events prior to localization. The interaction of low-energy electrons with surfaces and interfaces can be used to examine effects of high-energy radiation but with well-defined surface specificity. Several previous studies have employed ESD and high-energy photon stimulated desorption (PSD) to examine the neutrals<sup>38, 39</sup>, cations<sup>32, 40-43</sup>, and anions<sup>36, 44</sup> produced during the irradiation of ice. Extensive work by Sieger, et al., on the ESD of  $\text{D}^+$  from  $\text{D}_2\text{O}$  ice found phase effects and thresholds near 25, 40, and 70 eV corresponding to distinct electronically excited two-hole and two-hole one-electron states<sup>32</sup>. Velocity distributions of the protons showed

‘fast’ and ‘slow’ components with an interesting temperature dependence of the yield. Specifically, the yield of fast cations decreased with temperature and followed the work function change while the yields of slow cations increased with temperature<sup>32</sup>. A similar increase was also observed for the anion ( $D^-$ ) channel<sup>36</sup>. The data suggests the narrowing of  $a_1$  valence bands and increases in excited state lifetimes due to thermally activated reorientation of surface molecules and reduction in hydrogen bonding.

While electron-beam irradiation of ice primarily causes the desorption of  $H^+$ , other ions such as  $H_2^+$  and  $H^+(H_2O)_{n=1-8}$  are also produced<sup>32, 45, 46</sup>. Because all of these desorption products are sensitive to the local environments, a detailed study of these additional ESD products will provide further insight into the structure and dynamics of low-temperature ice surfaces.

## CHAPTER 2

### ULTRA-HIGH VACUUM (UHV) ENVIRONMENTAL CHAMBER

#### 2.1 Overview

The UHV chamber shown in Figure 2.1 was specifically designed for examining interfaces of environmental relevance. Briefly, the chamber consists of a liquid helium cryohead used to cool the rotatable sample which is located in the center of the chamber. A time-of-flight (TOF) mass spectrometer and a quadrupole mass spectrometer (QMS) are used as detectors on the chamber. The chamber is also equipped with a low energy electron gun and two dosing ports terminated in leak valves.

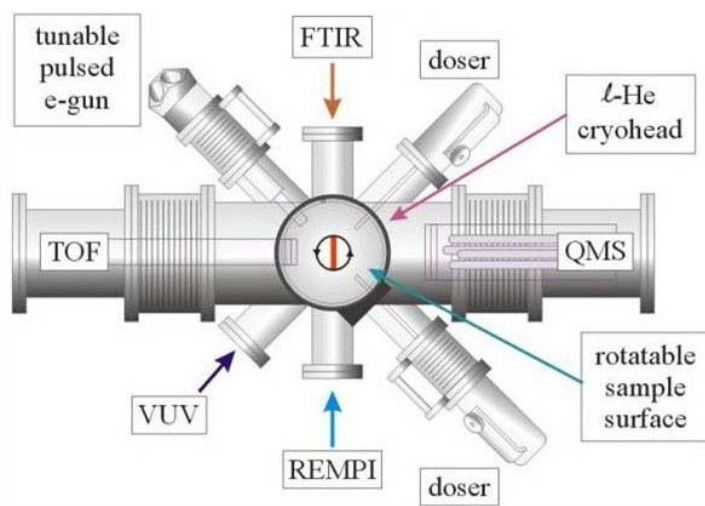


Figure 2.1 Schematic of UHV environmental surface science chamber

## 2.2 Sample

The cryohead is used to obtain the low temperatures required in UHV studies of ice surfaces. Copper shielding around the cooling tube is used to decrease the thermal radiation on the cooling stage and increase the effective cooling of the cryohead. Thermal connection to the sample is made through a copper block with tapped holes attached to the bottom of the cryohead. Low-oxygen copper was used due to its superior thermal conductivity. Electrical isolation was achieved by using a sapphire crystal. Sapphire has a high thermal conductivity at low temperatures, so it maintains good thermal contact with the cryohead but electrically isolates the sample. The sapphire crystal was sandwiched between two copper plates and the isolated copper plate was attached to the sample holder. The sample holder was designed with two thin drop-down legs to minimize the heat transfer to the copper connections and cryohead when the sample temperature was raised. It was important to maximize the contact between the zirconia oxide crystal used as a sample substrate and the copper sample holder in order to obtain the lowest possible sample temperature. Thin gold foil, which is malleable, was placed between the two metals to ensure good thermal contact. A resistive heater was employed to heat the sample. Nickel-chromium wire was wound in a coil which was placed inside of a ceramic tube. The ceramic tube was then wrapped in copper foil and mounted to the copper plate which was not electrically isolated so that the heater would be directly behind the sample surface. The ceramic tube was used to block the emitted electrons from reaching the sample. The nickel chromium wire was connected to copper wire and a UHV feed through flange to allow current to be run through the wire to

achieve the desired heating. The power supply used for heating was controlled by the computer and a suitable temperature calibration was achieved. The entire cryohead-sample assembly was mounted on a rotatable Conflat flange to allow the sample to rotate 360 degrees and face any port in the chamber.

### **2.3 Time-of-Flight (TOF) Mass Spectrometer**

The TOF was used to detect ion emission from the sample surface. The TOF was mounted on a translation stage and could be moved towards the sample surface. This allowed us to vary the flight distance of the ions and used mainly to calibrate the kinetic energy of the ions. When measuring spectra, the TOF was moved as close as possible to the sample surface ( $\sim 1$  inch) to maximize sensitivity. When recording TOF spectra, the sample was aligned perpendicular to the TOF. This maximized the detection efficiency and also allowed for velocity measurements of the desorbing ions. The ion optics of the TOF consisted of a top hat designed extractor with a fine mesh screen at the entrance. The mesh screen was used to ensure a uniform electric field. The 100 V extraction potential used was high enough to insure a large solid angle and rule out any discrimination against off-normal trajectories or ion angular distribution effects. The extractor voltage was pulsed on after the electron gun to collect the desorbing ions. After the ions were collected by the extractor, they were focused using a set of Einzel lenses before entering the flight tube. Voltages on these focusing lenses were varied to find the optimum collection efficiency. The ions finally impacted a multichannel plate detector which gave  $\sim 10^6$  gain of the signal. The signal was fed into an amplifier and recorded

using a multichannel scaler (MCS). The MCS allowed us to easily see small signals which required the addition of numerous spectra.

## **2.4 Electron Gun**

The low energy electron gun irradiates the sample producing the ions measured by the TOF. The electron gun is at a 45 degree angle to the sample surface and is positioned as close as possible alongside the TOF extractor. The electron beam is focused on the center of the sample surface and pulsed with electron energies ranging from 5 – 400 eV. Typical operating conditions were  $\sim 10^{13}$  electrons/s/pulse or time averaged currents of  $\sim 100$  pA. Images of the sample are taken at different electron energies by rasting the beam in the x and y directions and measuring the resulting current on the sample. The current will be high when the electron beam is on the surface and negligible when the beam is not focused on the surface. Images clearly showing the sample are obtained for different focusing conditions to obtain the best conditions for different energies. These images provide the coordinates and settings for focusing different energy electrons onto the sample surface.

## **2.5 Pulsing Sequence**

The electron gun and TOF extraction grid were pulsed using a pulse generator. The pulsing conditions were varied to maximize the signal intensity without charging the sample surface. The pulsing sequence was set at 500 Hz and consisted of a 200 ns pulse



delivered to the electron gun followed immediately by a 100  $\mu$ s extraction pulse. The extraction pulse was applied just after the end of the electron pulse to avoid the influence of the potential field on the electron energy. This pulsing sequence allowed the sample to discharge before the next pulse of electrons.

## **2.6 Quadrupole Mass Spectrometer (QMS)**

Neutral molecules were measured using a quadrupole mass spectrometer, which was mounted opposite of the TOF spectrometer. Temperature programmed desorption measurements were taken with the QMS and it was also used to monitor contamination while dosing. The Extrel QMS consisted of an ionizer region where electrons of 70 eV are generated and ionize the neutral molecules. The newly ionized species are then focused by a set of Einzel lenses before entering the quadrupole chamber. An Extrel Model 13 High-Q head is used to deliver a oscillating radio frequency (RF) with a constant DC potential to the four parallel rods in the QMS. Variation of the RF frequency changes the mass to charge ( $m/z$ ) ratio that is in resonance and reaches the detector. By supplying a sweeping input voltage a mass spectrum is obtained from 1 - 60 amu. The applied voltages (0 - 10 V) supplied to the input of the QMS controller correspond to specific masses. These voltages were calibrated by recording the mass spectrum after dosing several known gases individually and noting the change in the specific peak heights corresponding to the mass of the dosed gases. After calibration, the QMS was controlled by a LabView program which could take an entire mass spectrum by sweeping the input voltage or monitor a specific mass by applying a constant voltage.

This program was also designed to control the heater voltage and could ramp the temperature while monitoring up to 6 masses, recording each temperature desorption trace. The temperature programmed desorption measurements were taken with a temperature ramp rate of 1.5 K/s. The dose rate and coverages were calibrated relative to known temperature programmed desorption (TPD) profiles from water adsorbed on Pt(111). Due to the large signal for the water doses employed, the water signal was monitored at  $\sim 1/100$  of the maximum signal intensity. HCl desorption was monitored at  $m/z$  36 and calibrated using the corrected ionization efficiency of HCl relative to water.

## 2.7 Dosing System

The vapor dosing system designed for the environmental chamber is made of two separate dosing lines to avoid any cross contamination between the species being studied. It is especially important to avoid water contamination when studying ionization reactions as the contamination may provide false evidence of ionization. To this end, each dosing line is equipped with a liquid nitrogen trap and is terminated in a leak valve attached to the main chamber.

Specifically, the H<sub>2</sub>O (D<sub>2</sub>O) is contained in a glass bulb separated from the dosing line by a Swagelok valve. The nanopure H<sub>2</sub>O is purified by several freeze-pump-thaw cycles to remove any dissolved gasses, and care is taken to ensure the dosing lines are fully passivated with the water vapor by several cycles of saturating and evacuating. The leak valve used for water dosing was mounted on a translation stage that could be moved towards the center of the chamber. The leak valve was fitted with a stainless steel tube of

~ 0.25 inch diameter for directed dosing of the sample. This setup allowed dosing of the sample from a distance of ~ 0.5 inches, increasing the effective dosing and decreasing the background dosing of the chamber. Several types of ice can be dosed by varying the substrate temperature while dosing or annealing the ice samples created at low dosing temperatures. Specifically, porous amorphous solid water (PASW), amorphous solid water (ASW), and crystalline ice (CI) were used in the low temperature ice studies. Porous amorphous ice is characterized with a high surface to volume ratio and can be dosed at temperatures  $\leq 80$  K<sup>47-49</sup>. In this temperature range, the water molecules ‘hit and stick’ with random orientations, and off-normal dosing trajectories can create highly porous ice samples<sup>47</sup>. Dosing water vapor at higher temperatures creates amorphous solid water, occurring around 110 K. The water molecules remain randomly oriented in the ice bulk, however ASW is not porous. The collapse of the pores as the temperature increases from 80 K to 120 K causes an irreversible increase in the cation yields associated with a decrease in the surface roughness of the ice film<sup>50</sup>. Crystalline ice is made by dosing at temperatures  $\geq 140$  K, and lower temperature ice annealed to temperatures  $\geq 140$  K forms polycrystalline ice<sup>51</sup>. The CI samples grown here are most likely polycrystalline, with a well-ordered hydrogen bond network in crystallites. Grain boundaries in CI form where two or more crystallites meet. These grain boundaries can play important roles in diffusion due to the increased number of dangling bonds and the break in the hydrogen bonding network.

The HCl dosing line was also thoroughly flushed, as the HCl can react with the stainless steel and produce contamination in the line. The HCl leak valve was fitted with a glass dosing tube for directed dosing. Initially H<sub>2</sub> was measured as the main component

in the HCl dosing line with the QMS. After several days of flushing, the HCl dosing line was passivated and HCl was dosed free of contamination.

## CHAPTER 3

### ELECTRON-STIMULATED DESORPTION OF CATIONS FROM PRISTINE ICE SURFACES

#### 3.1 Overview

Low-energy (5 - 250 eV) electron stimulated desorption (ESD) has been used to study the production and removal of  $\text{H}_2^+$  and protonated water clusters ( $\text{H}^+(\text{H}_2\text{O})_{n=1-8}$ ) from porous amorphous solid water (PASW), amorphous solid water (ASW), and crystalline (CI) water ice films. The threshold energy for ESD of  $\text{H}_2^+$  from CI and  $\text{H}_3\text{O}^+$  from PASW and ASW is  $\sim 22 \pm 3$  eV. There is also a  $\text{H}_2^+$  yield increase at  $\sim 40 \pm 3$  eV and a  $\sim 70 \pm 3$  eV threshold for ESD of  $\text{H}^+(\text{H}_2\text{O})_{n=2-8}$  from PASW and ASW.  $\text{H}_2^+$  production and desorption involves direct molecular elimination and reactive scattering of an energetic proton. Both of these channels likely involve localized two-hole one-electron and/or two-hole final states containing  $4a_1$ ,  $3a_1$  and/or  $2a_1$  character. The 70 eV cluster ion threshold implicates either an initial ( $2a_1^{-2}$ ) state localized on a monomer or the presence of at least two neighboring water molecules each containing a single hole. The resulting correlated two-hole or two-hole, one-electron configurations are localized within a complex and result in an intermolecular Coulomb repulsion and cluster ion ejection. The  $\text{H}^+(\text{H}_2\text{O})_n$  yields are highest from PASW relative to ASW and CI and decrease with temperature, whereas the  $\text{H}_2^+$  yields are highest for CI and increase with temperature. The temperature effects and cluster ion distributions are accounted for by

distance and temperature dependent hole screening. Changes in screening, hole lifetimes and hopping probabilities are greatest for  $a_1$  levels. This is supported by valence band photoemission studies of ice as a function of temperature.

### 3.2 Experimental Details

The techniques and apparatus have been developed to examine non-thermal processes at interfaces and have been described in detail in Chapter 2. Briefly, the experimental system consists of an ultra-high vacuum chamber (base pressure  $2 \times 10^{-10}$  Torr) equipped with a rotatable helium-cooled sample mount, a pulsed low-energy (5-250 eV) electron gun, a time-of-flight (TOF) and a quadrupole mass spectrometer (QMS). The ice was grown on an oxidized zirconium or Pt(111) substrate mounted in thermal contact with the helium compressor, and radiatively heated by a tungsten filament. The surface temperature was monitored with a type-K thermocouple spot-welded to the substrate and the range studied was 80 – 600 K. A computer-controlled feedback system drove the temperature ramp, which was 8 K/min for both temperature-programmed desorption (TPD) and ESD ion yields vs. temperature measurements.

The pulsed electron beam supplies a time-averaged electron flux of about  $6 \times 10^{13}$   $\text{e}^- \text{cm}^{-2} \text{sec}^{-1}$ , in a spot size of roughly  $0.5 \text{ mm}^2$ . The low incident current precludes any beam-induced heating, gas phase interactions and any appreciable surface charging<sup>52</sup>. The incident electron energy,  $E_i$ , could be varied continuously from 5 to 250 eV, with an energy spread of  $\sim 0.3$  eV. The electron beam incident angle was  $45^\circ$  with respect to the surface normal. Ions desorbing as a result of electron impact on the ice surface and

interface were collected using a TOF spectrometer mounted perpendicular to the sample surface and along the surface normal direction. TOF spectra were obtained within minutes using a transient digitizer. Typical conditions involved 65,000 sweeps/averages and a 100 V extraction field applied to the TOF grid. The use of an extraction field insures total ion collection but disrupts measurements of ion velocity distributions. Due to signal intensities, the velocity distributions of  $\text{H}_2^+$  and some cluster ions were obtained under nearly field free conditions. The velocity distribution of the strong proton signal was obtained under field-free conditions and all TOF distributions were converted to kinetic energy distributions using the appropriate Jacobian transformation.

Water condensation at temperatures below 100 K forms microporous amorphous ice<sup>48, 49</sup>. This is referred to as porous amorphous solid water (PASW), which is characterized by a high surface area ( $\sim 640 \text{ meter}^2/\text{g}$ )<sup>47</sup> and low density. Sintering microporous ice between 100 - 120 K or deposition at temperatures between 110 - 130 K generates normal (non-porous) amorphous ice or simply amorphous solid water (ASW). Films grown above 140 K form either hexagonal crystalline ice Ih(0001) or cubic crystalline ice Ic(001), which we refer to as simply crystalline ice (CI). Amorphous ice annealed at 150 K undergoes a phase transition to polycrystalline ice<sup>51</sup> and sublimates rapidly in vacuum above 165 K. The samples we have studied in this experiment were PASW, ASW or CI. Water coverages were calibrated relative to TPD of water on Pt(111) and fresh ice samples were deposited after every 3 - 4 spectra to minimize any affects due to surface charging.  $\text{D}_2\text{O}$  as well as  $\text{H}_2\text{O}$  were used to verify mass and velocity assignments though all ESD data presented was obtained with  $\text{H}_2\text{O}$ . All data was obtained at coverages  $> 50 \text{ ML}$  to minimize substrate mediated effects.

The photoemission studies were carried out by Dr. Matthew Seiger on a separate ultrahigh vacuum system at the Wisconsin Synchrotron Radiation Center. The UHV system was equipped with a double pass hemispherical analyzer and a 55 eV photon energy was used. This photon energy was chosen to minimize the photoelectron mean-free path and maximize surface sensitivity. Samples were either 50 ML of H<sub>2</sub>O or D<sub>2</sub>O ASW or CI grown on a resistively heated Cu(111) surface. Data was taken as a function of temperature and the zero energy photoelectron position was determined relative to the Fermi-level position of the underlying Cu substrate.

### 3.3 Results

#### 3.3.1 Time-of-Flight (TOF) Spectra

Figure 3.1 shows the 250 eV ESD-TOF yield of H<sub>2</sub><sup>+</sup> and H<sup>+</sup>(H<sub>2</sub>O)<sub>n</sub> clusters as a function of the phase of ice. Also included is data for H<sup>+</sup> which provides a very useful basis for comparing the yields and kinetic energy distributions. PASW (bottom panel) grown at 80 K has the largest cluster signal with n as large as 9 produced (not shown), and CI (top panel) has the smallest yield. The yield of ASW (middle panel) is between PASW and CI. It is important to note the scaling factors in the TOF spectra in Figure 3.1. The H<sub>2</sub><sup>+</sup> yields are factors of 20, 50, and 50 less than the H<sup>+</sup> yield from PASW, ASW and CI, respectively. The cluster ion yields are factors of ~ 40, 150 and 300 less than the H<sup>+</sup> yield from PASW, ASW and CI, respectively. The approximate ratios of the



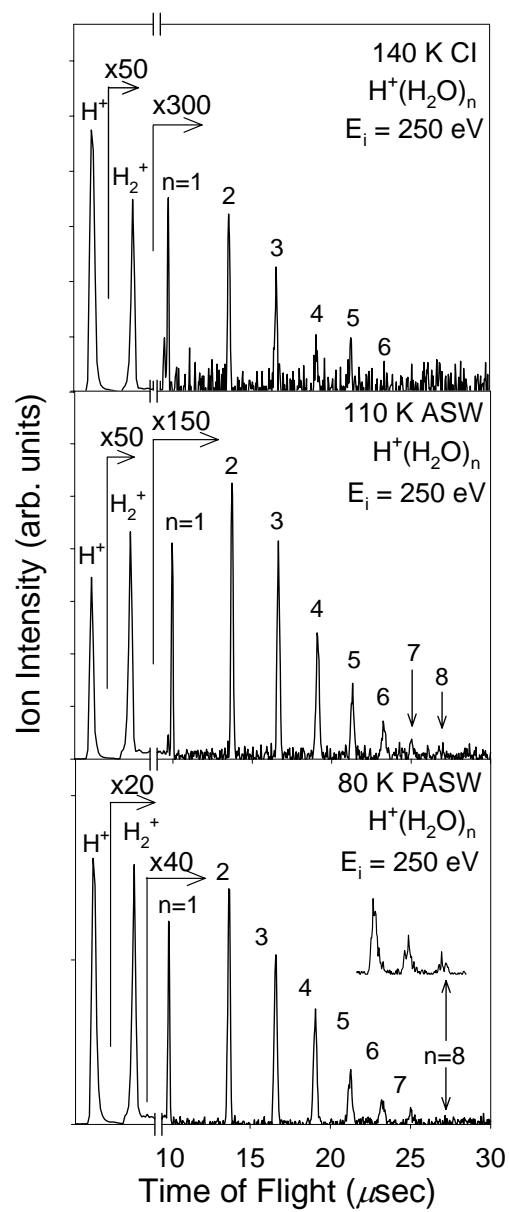


Figure 3.1 ESD-TOF from  $\sim 50 \text{ ML}$  of CI, ASW, and PASW

cluster yields are 1:2:6 for CI, ASW and PASW ice respectively. It is important to note that the  $m/z = 2$  signal is not pure  $H_2^+$ .

The  $H^+$ ,  $D^+$ ,  $H_2^+$  and  $D_2^+$  signals exhibit the opposite phase dependence as the clusters. Specifically, the yield of all these species is higher for crystalline ice relative to the amorphous ices. Ice samples that were either grown at 140 K or grown at 80 K and annealed to 140 K both show high  $H^+$ ,  $D^+$ ,  $H_2^+$  and  $D_2^+$  yields. The elevated yield for CI persists at low temperature, as expected; the sample remains crystalline once formed. The  $H^+$  ( $D^+$ ) signal ratio is approximately 3:2:1 while the  $H_2^+$  ( $D_2^+$ ) signal is 1.5:1:1 for CI, ASW and PASW, respectively.

### 3.3.2 Cation ESD Threshold Energies

Direct information regarding the electronic configurations giving rise to the ESD of cations can be obtained from threshold measurements. The threshold measurements shown here were taken from the form of ice which gave the largest yield to ensure the greatest sensitivity. The threshold energies for ESD of  $H_2^+$  and  $H^+(H_2O)_{n=1-3}$  are shown in Figure 3.2A for CI and Figure 3.2B for PASW, respectively. The data is represented in by symbols; frame 3.2.A and inset: (●)  $H_2^+$ , frame 3.2.B and inset: (●)  $H^+(H_2O)$ , (▽)  $H^+(H_2O)_2$ , and (■)  $H^+(H_2O)_3$ . Guidelines are also included in the figure strictly as a guide to the eye and are not representative of an equation or fit to the data. Note the scale for CI (A) is approximately 33 times that of PASW (B) due to the lower yield of the cluster ions. Notice the scale for Figure 2B (PASW) has been multiplied by  $\sim 33$  compared to

the scale for Figure 3.2A (CI) emphasizing the difference in yields due to the phase and temperature. The  $\text{H}_2^+$  yield inset in Figure 3.2A has been multiplied by  $\sim 66$  compared to the full scale CI data and the  $\text{H}^+(\text{H}_2\text{O})_{n>1}$  inset in Figure 3.2B has been multiplied by 7. The proton threshold is not shown but is 22 eV and is exactly the same as previously reported data<sup>32</sup>.

This threshold energy has been assigned to several localized two-hole one-electron states and is discussed in more detail in Section 3.4. The ESD of  $\text{H}_2^+$  also has a threshold near 22 eV with an additional increase  $\sim 40$  eV (Figure 3.2A). There is also a small  $\text{H}_3\text{O}^+$  yield  $\sim 22$  eV, and an increase in the yield of all cluster ions at  $\sim 70$  eV (see Figure 3.2B). The low threshold energy is not observed for clusters with  $n > 1$ . In view of the fact that the  $n = 2$  signal is nearly as strong as the  $n = 1$  signal, the lower threshold energy indicates that the formation and desorption of  $\text{H}_3\text{O}^+$  involves multiple mechanisms. Due to the lower cluster yield in crystalline ice, the threshold energies were difficult to determine. However, a primary threshold energy near 70 - 90 eV seems to be present. Our estimated detection sensitivity brackets the threshold data to desorption events which have ESD cross sections of  $> 10^{-21} \text{ cm}^2$ .

### 3.3.3 Kinetic Energy Distributions

The kinetic energy distributions of the desorbing cations are shown in Figures 3.3 and 3.4. In order to determine accurate velocity distributions, the ESD proton velocity was determined under field free conditions and with the sample in a normal take-off

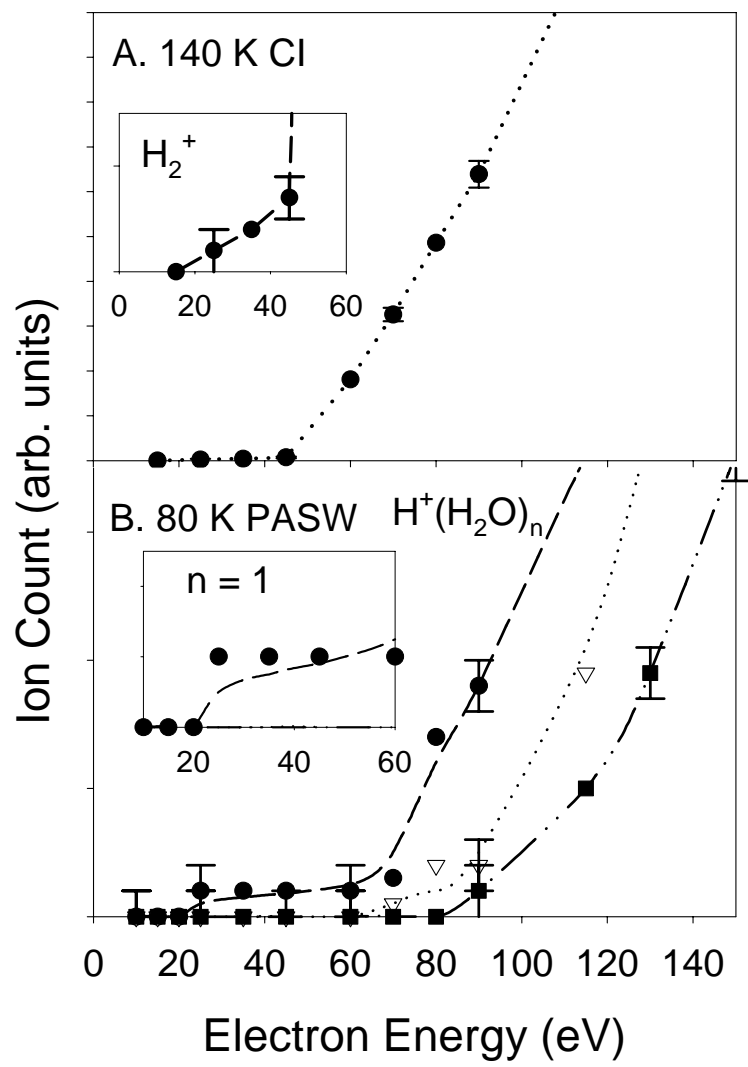


Figure 3.2 ESD threshold measurements of  $\text{H}_2^+$  and water clusters ( $\text{H}^+(\text{H}_2\text{O})_{n=1-3}$ )

geometry relative to the TOF detector. The TOF spectra taken under these field free conditions can be converted into a kinetic energy distribution by using the Jacobian transformation  $I(E) = I(t)t^3/(mL^2)$  and are shown in Figure 3.3. The kinetic energy distribution of  $H^+$  from 50 ML CI and PASW during pulsed irradiation with 250 eV electrons under field free conditions is shown. The data points ( $\bullet$  - CI,  $\square$  - PASW) show the Jacobian transformation of the raw velocity distribution data which are fitted using Gaussian distributions (dashed and solid lines). Previous measurements of the proton

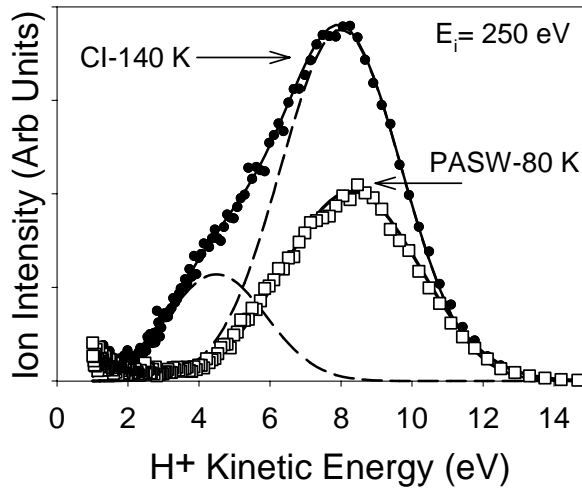


Figure 3.3 Proton kinetic energy distributions from CI and PASW

kinetic energy were performed using a non-normal take-off geometry and an extraction potential<sup>32</sup>. This led to the assignment of ‘fast’ and ‘slow’ protons without an assignment of the kinetic energies. Figure 3.3 shows that, using incident electron energies of 250 eV, the proton kinetic energy is peaked at  $\sim 8.5$  eV with a Gaussian-like distribution which extends from 4 - 14 eV. These energies are similar to those previously reported by Stulen

and Noell<sup>53</sup> though at these high incident electron energies, the low energy feature near 4 eV only becomes more noticeable for higher ( $> 120$  K) temperatures. This is shown in the velocity distribution obtained at 140 K.

The velocity distributions of the clusters cannot be measured under field free conditions due to the low signal intensities and broadening. However, the  $\text{H}^+$  and  $\text{H}^+(\text{H}_2\text{O})_n$  distributions were measured using several low extraction voltages (4 , 6 , and 10 V). Figure 3.4A shows the measured distributions of  $\text{H}^+$  and  $\text{H}^+(\text{H}_2\text{O})_{n = 1-3}$  from PASW at 80 K using 250 eV electrons and a 10 V extraction field. The symbols are the Jacobian transformation of the raw data,  $\text{H}^+(\bullet)$ ,  $\text{H}^+(\text{H}_2\text{O}) (\square)$ ,  $\text{H}^+(\text{H}_2\text{O})_2 (\circ)$  and  $\text{H}^+(\text{H}_2\text{O})_3 (\blacktriangle)$ , with a Gaussian fit to the data shown by the dashed (clusters) and solid ( $\text{H}^+$ ) lines. The clusters  $n = 1 - 3$  each have the same kinetic energy distributions. To estimate the kinetic energy distributions in zero field, the Gaussian fits to the data were corrected for the extraction voltage by comparison to the proton data which was measured under both conditions. The kinetic energy distribution obtained using the Gaussian fits that have been extrapolated to zero extraction field are shown in Figure 3.4B. The clusters have a lower mean kinetic energy, estimated to be  $\sim 5 \pm 1$  eV. Typically, the kinetic energy of departing fragments can shift due to charge build-up and have been used as probes for charging<sup>52</sup>. The total dose used in this study is  $< \sim 10^{13} \text{ e}^- \text{ cm}^{-2}$  and is not expected to lead to any measurable charging<sup>52</sup>.

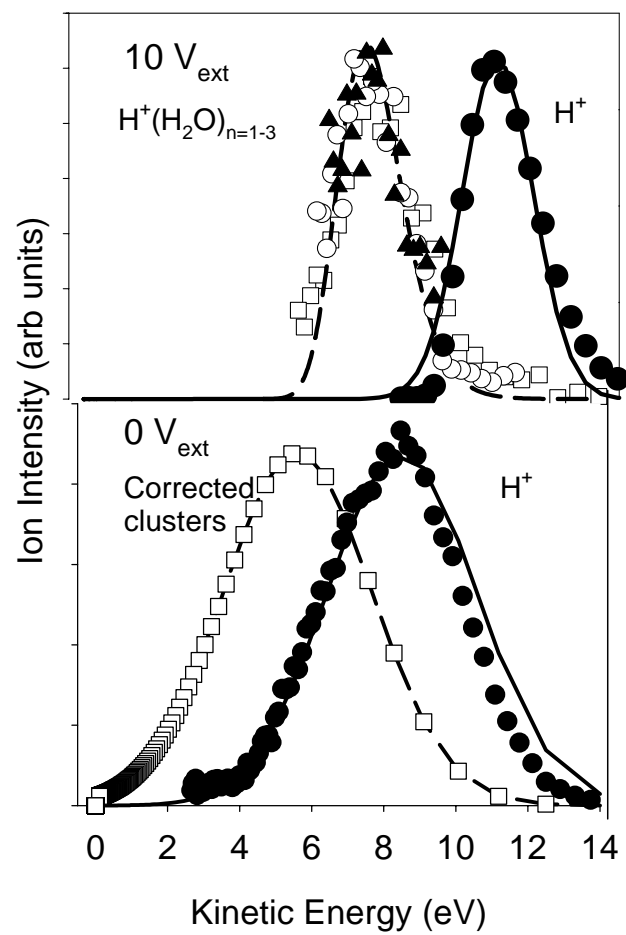


Figure 3.4 Measured and calculated kinetic energy distributions of proton and cluster ions from PASW

### 3.3.4 Temperature Dependent Yields

As shown in Figure 3.5, the ESD cation yields are very sensitive to the substrate temperature with all changes in the  $\text{H}_2^+$  and  $\text{H}^+(\text{H}_2\text{O})_n$   $n=1-3$  yields occurring before the thermal desorption of  $\text{H}_2\text{O}$ <sup>45</sup>. In Figure 3.5, the symbols represent the yield of (●)  $\text{H}_2^+$ , and  $\text{H}^+(\text{H}_2\text{O})_n$ ,  $n=(\circ)$  1, ( $\triangle$ ) 2, ( $\square$ ) 3 from 50 ML water dosed at 80 K and irradiated with a pulsed beam of 250 eV electrons. The inset shows a temperature programmed desorption of water, indicating the ESD yields change before the onset of thermal desorption. The cluster signal drops when the temperature is raised from 80 K (the low-temperature limit with the current setup) but reaches a minimum and plateau around 140 K. Conversely, the  $\text{H}^+$  and  $\text{H}_2^+$  begin to increase at temperatures above 110 K. This increased yield reaches a maximum value at 150 K and then drops when the sublimation rate increases. This temperature dependence is very similar to previous observations for proton ESD (see Fig 3 in Sieger. et. al.)<sup>32, 45</sup>. As discussed later in Section 3.4, the cation ESD yields are related to the number of dangling bond sites and the type of donor-acceptor configurations at the surface. The temperature dependence is related to the change in the hydrogen-bonding environment of the surface and interface molecules. The change in the hydrogen bonding can effect screening and also lead to the onset of surface diffusion and lateral motion.



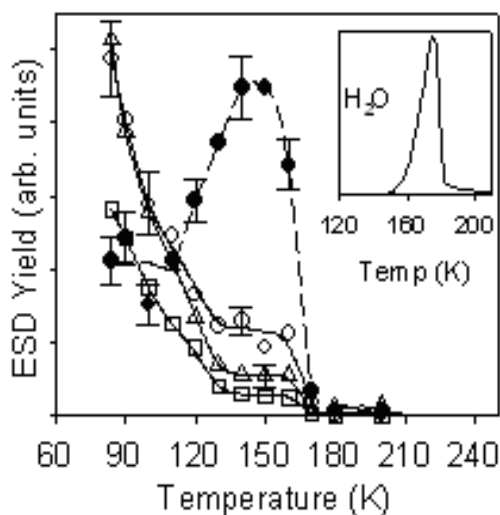


Figure 3.5 Temperature dependence of ESD cation yields from ice, inset shows temperature programmed desorption of water.

### 3.4 Discussion

#### 3.4.1 Electronic Structure of Ice

Prior to discussing the mechanisms of cation ESD and the implications of the temperature dependencies, the relevant facts concerning the electronic structure of water are summarized. Photoemission data which probes the shallow core or inner valence region of interest to this work is also presented. Briefly, the ground state of an isolated water molecule is  $(1a_1)^2(2a_1)^2(1b_2)^2(3a_1)^21(b_1)^2$ . The molecular orbital diagram of water is shown in Figure 3.6. The  $2a_1$  is the inner valence orbital with mostly O 2s character, the  $1b_2$  is strongly bonding, the  $3a_1$  has both bonding and lone-pair character and the  $1b_1$

is a non-bonding lone pair orbital. The O-H bond is mainly composed of the  $1b_2$  and  $2a_1$  orbitals, the  $1b_1$  and  $3a_1$  contribute to the oxygen lone-pair orbitals, and the lowest unoccupied molecular orbitals are the  $4a_1$  and  $2b_2$ . These unoccupied levels, particularly the  $4a_1$ , are strongly antibonding and lead to O-H bond breakage if occupied.

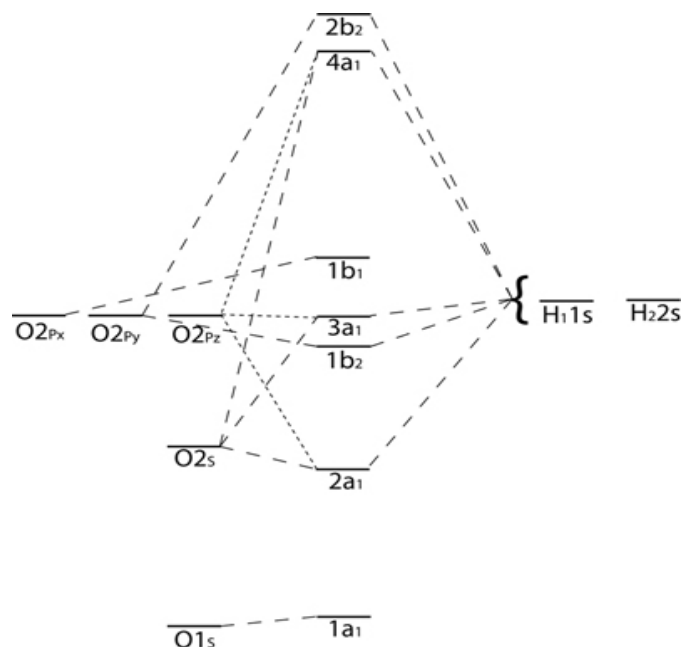


Figure 3.6 Molecular orbital diagram of water

The molecular orbitals of condensed ice retain much of their gas-phase character with some broadening and minor shifting of the energy levels<sup>54, 55</sup>. Peaks in the valence band density of states are therefore labeled with the same notation as the free molecule. The valence band photoemission spectra of 40 ML of ASW and CI on Cu(111) using  $h\nu = 55$  eV are shown in Figure 3.7. The main features have been assigned to the  $2a_1$ ,  $1b_2$ ,  $3a_1$ , and  $1b_1$  levels and are referenced to the Fermi level of the underlying Cu substrate.

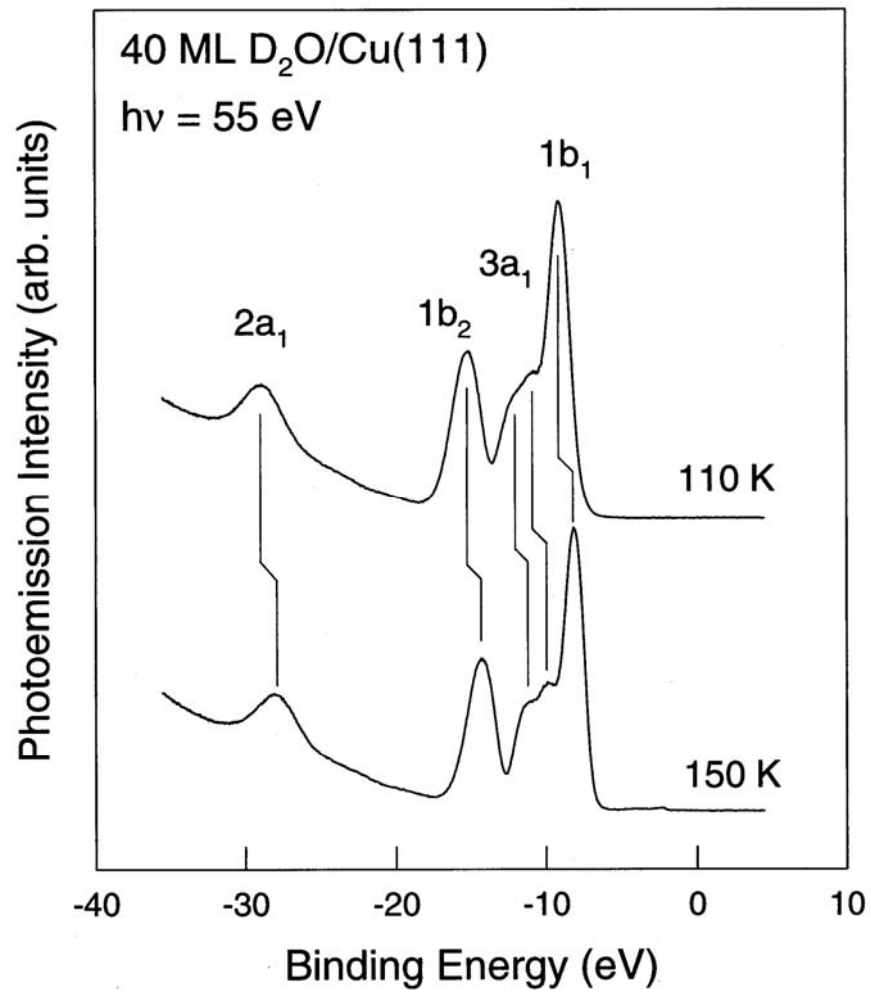


Figure 3.7 Photoemission spectra of ASW and CI

There is also a narrow conduction band that is composed primarily of the  $2b_2$  level that extends about 1 eV below the vacuum level and about 8 eV above the  $1b_1$  band maximum (not shown). The photoemission data makes it clear that the  $a_1$  levels broaden in the solid state and are strongly affected by hydrogen bonding. There is also an overall reduction in the intensity of the  $1b_2$  band (relative to the gas-phase) and shift in the binding energies of all bands as ASW transforms to CI. The latter is primarily due to the change in the value of the work function as the ice crystallizes<sup>56</sup>.

Figure 3.7 also shows that the broadening associated with the  $3a_1$  level emerges into a well-defined splitting as the temperature of the ice is increased. The  $3a_1$  molecular orbital is composed primarily of the lone pair orbitals of oxygen and is strongly involved in hydrogen bonding. Thus it is very sensitive to the local geometry of the nearby water molecules. The splitting and narrowing of the  $3a_1$  level is likely due to the reduced perturbation on the  $a_1$  levels and the return of the atomic  $p_z$ -character as the number of hydrogen bonds changes<sup>57</sup>. For a symmetric pair of water molecules in a unit cell of ice, the  $3a_1$  orbitals directly interact with each other giving rise to a bonding and antibonding combination. The presence and onset of this splitting is a very useful probe of rehybridization and local changes in the hydrogen bonding network. This view is also supported by a recent study of liquid phase water using x-ray emission spectroscopy<sup>58</sup>.

It is well known that water can dissociate upon non-thermal activation which includes excitation by ultraviolet light<sup>59</sup>, low-energy electrons<sup>25, 32, 40, 50</sup> and x-rays<sup>60</sup>. In fact, very facile x-ray induced dissociation of the first water layer on Ru(001) was recently found<sup>60</sup>. This was largely attributed to the secondary electrons produced by the high energy x-rays and the multiple scattering which occurred at the interface.

Ultraviolet photoemission studies on thin-films of water using photon energies similar to those used in our studies are known to produce much less damage. In addition, concurrent features which can be attributed to the  $3\sigma$  and  $1\pi$  levels of  $\text{OH}^-$  at 11.3 and 7.2 eV (relative to the Fermi level) respectively, have been used as indicators of beam damage<sup>59</sup>. There is no evidence of any feature at 7.2 eV, thus ruling out the formation of significant amounts of  $\text{OH}^-$  during the course of our photoemission measurements. In addition, the  $3a_1$  splitting is observed immediately when ice is grown at 155 K. This feature is not temperature dependent on crystalline ice and can not be due to beam damage<sup>61</sup>.

### 3.4.2 Mechanism of $\text{H}^+$ Desorption

The  $\text{H}^+$  yield shows a linear response to flux indicating single electron impact events. The threshold data and the effects of phase and temperature on kinetic energy distributions and yields are consistent with our previous measurements<sup>32, 40</sup>. There are four primary valence configurations known to produce protons with kinetic energies ranging from 0 to  $> 7$  eV<sup>41, 53</sup> shown in Figure 3.8. These two-hole and two-hole one electron excited states have excitation energies ( $E^*$ ) from 21 -  $\sim 70$  eV. The valence configurations  $(3a_1)^{-1}(1b_1)^{-1}(4a_1)^1$  and  $(3a_1)^{-2}(4a_1)^1$  require 21 - 25 eV and 31 - 36 eV excitation energies respectively and both produce protons with kinetic energies from 0 - 4 eV. These are referred to as ‘slow protons’<sup>32</sup>. The  $(1b_1)^{-2}(4a_1)^1$  configuration requires 26 - 31 eV and produces protons with 4 - 7 eV kinetic energy. The two-hole  $(2a_1)^{-2}$  state

requires 70 eV and produces ‘fast protons’ with kinetic energies of over 7 eV. Direct ionization of a single-hole ( $2a_1$ )<sup>-1</sup> state requires 25 eV and could also produce protons<sup>39</sup>.

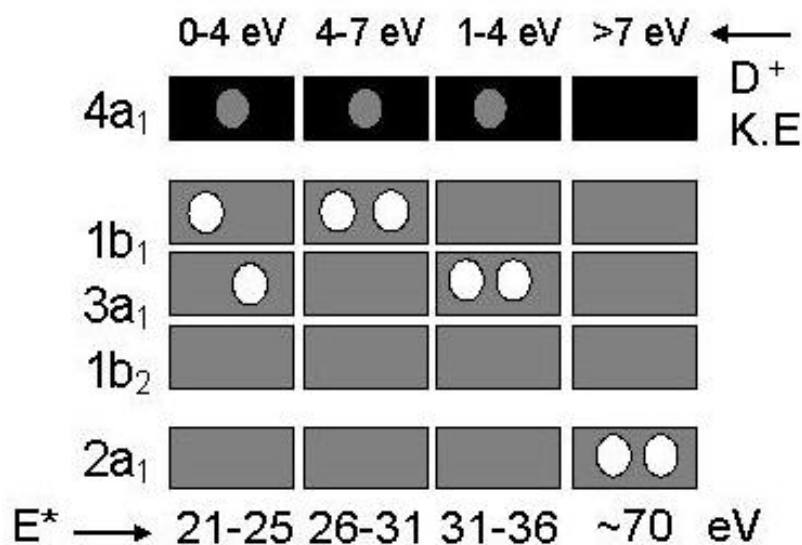


Figure 3.8 Two-hole and two-hole one-electron configurations of water

In general, the kinetic energy of the protons is mainly due to the Coulomb repulsion of the holes localized within a molecule, although the  $4a_1$  and  $2b_2$  levels are dissociative.

The above assignments were made primarily based upon previously reported *ab initio* configuration interaction calculations<sup>41, 62, 63</sup>. At the surface of ice, the above-mentioned two-hole, one-electron states can also have some  $2b_2$  character with the admixture dependent upon the number of donor hydrogen bonds<sup>57</sup>. In fact, all of these multi-electron states are likely to be of mixed character. Thus, the assignments only indicate the likely dominant electronic configurations. At low temperatures, the multihole configurations which do not contain  $3a_1$  or  $2a_1$  character are most important.

### 3.4.3 Mechanism of $\text{H}_2^+$ Desorption

The molecular hydrogen ion yield is significantly lower than the proton yield however it has similar threshold values. Straub et al.<sup>64</sup> have measured the partial cross section for producing  $\text{H}^+$  and  $\text{H}_2^+$  via  $\text{H}_2\text{O}$  dissociative ionization in the gas phase. At 30 eV, production of  $\text{H}^+$  has a partial cross section  $> 100$  times that of  $\text{H}_2^+$ . For 250 eV electrons, the partial cross section for  $\text{H}^+$  production is  $> 200$  times that of  $\text{H}_2^+$ . The formation of  $\text{H}_2^+$  has also been reported in resonant photoionization of water at the oxygen  $K$  edge<sup>65</sup>. This was concentrated near the  $\text{O } 1s \rightarrow 2b_2$  resonance and was associated with the excitation of a highly excited bending mode<sup>65</sup>. A recent multiphoton ionization study found an excited ion state that produced  $\text{H}_2^+$  ( $X^1\Sigma_g^+$ ) directly via molecular elimination<sup>66</sup>. This state was produced after the water ion absorbed four 532 nm photons. The only states within the doublet system of the water ion that can have  $\text{H}_2^+$  ( $X^1\Sigma_g^+$ ) as a dissociation product are  $X^2B_1$  and the excited  $B^2B_2$ . The formation of  $\text{H}_2^+$  was attributed to non-adiabatic dissociation of the water ion through one of these two excited states.

The two-hole one-electron or two-hole states previously discussed as the primary source of protons can decay via pathways that result in the formation of  $\text{H}_2^+$ . Although the overall contribution is low due to its small branching fraction ( $2 \times 10^{-3}$  in gas phase water), this has been observed in the time correlated dissociation of doubly ionized states of water<sup>67</sup>. The process is not observable in single photon studies implying the potential role of inaccessible dissociative *triplet* states. The relatively high yield of  $\text{H}_2^+$  observed in our studies relative to previous gas-phase studies argues for additional pathways and/or

many body interactions. Several possibilities exist which can enhance the yield of  $\text{H}_2^+$ . These include multiple scattering of incoming and outgoing electrons, increased cross sections for exciting triplet states and reactive scattering of energetic protons. In this work, the weak threshold energy at 22 eV can correlate with the  $(1b_1)^{-2}(4a_1)^1$  and  $(3a_1)^{-1}(1b_1)^{-1}(4a_1)^1$  states. The 40 eV threshold can correlate with either the  $(3a_1)^{-2}(4a_1)^1$ ,  $(1b_2)^{-1}(3a_1)^{-1}(4a_1)^1$  and  $(1b_2)^{-2}(4a_1)^1$  states or direct double ionization to produce  $(1b_2)^{-2}$  or  $(1b_2)^{-1}(3a_1)^{-1}$  or  $(3a_1)^{-2}$  two-hole states. The vertical double ionization transition to the ground state of  $\text{H}_2\text{O}^{2+}$  ( $^3\text{B}_1$  in  $\text{C}_{2v}$  symmetry or  $^3\Sigma_g^-$  in linear symmetry) was predicted to appear at 39.2 eV. The dissociation limit for formation of  $\text{H}_2^+ + \text{O}^+$  from direct double ionization of water is 34.1 eV; a value within our threshold measurement limits. The vertical double ionization potential has been calculated to be only 30.15 eV for the water dimer<sup>68</sup>. Double ionization of an orientational D-defect configuration (i.e. a dimer configuration present in ice with hydrogen bonds pointing toward one another), could lead to direct  $\text{H}_2^+$  production while leaving behind a  $\text{H}_2\text{O}^+ - \text{O}$  or  $\text{HO}^+ - \text{OH}$  fragment.

The electron flux dependence of  $\text{H}_2^+$  formation is also linear thus implying a mechanism involving a single electron-impact event. This is consistent with direct formation via a molecular elimination channel either from a single terminal water molecule or a more complex structure such as a dimer. It is also possible that reactive scattering of an energetic proton can strip away a hydrogen atom and produce  $\text{H}_2^+$ . This process would also be consistent with a linear flux dependence providing the scattering event involves a preformed dimer or more highly coordinated cluster. Since all terminal water molecules on an ice surface are hydrogen bonded to at least one or two water



molecules, this criteria is always fulfilled. The kinetic energies of the  $\text{H}^+$  and  $\text{H}_2^+$  are also very close, thus it is difficult to rule out this channel.

#### 3.4.4 Mechanism of Cluster Ion Desorption

The production of charged water clusters from ESD of water ice has been seen as early as 1972 by Floyd and Prince<sup>69</sup>. Water clusters of the formula  $\text{H}^+(\text{H}_2\text{O})_n$  ( $3 \leq n \leq 8$ ) were attributed to ‘clustering about an energetic proton fragment’<sup>70</sup>. These early studies were performed at high temperatures, 153 K and 193 K. Since water sublimates in vacuum at these temperatures, the data likely contains significant contributions from the gas phase. No results were obtained for ice at 77 K most likely due to their lack of sensitivity. More recently there have been reports of water clusters from nanoclusters of water adsorbed on graphite<sup>71</sup>, rare gases<sup>72</sup>, condensed molecular ices<sup>39</sup> and ionic substrates<sup>73</sup>. Water clusters composed of 1 - 2 water molecules were also observed during vacuum ultraviolet irradiation of water on graphite at 80 K<sup>71</sup> and the mechanism was attributed to reactive scattering of an energetic proton. A mechanism involving a Coulomb explosion between localized holes within or on a cluster was presented by Souda<sup>72</sup> to explain the large cluster yield from nanoclusters adsorbed on rare gases. In the case of multilayers of water, a model based upon two-hole localization on a single water or pair of water molecules followed by a Coulomb repulsion mechanism was presented<sup>45</sup>.

The weak threshold for  $\text{H}^+(\text{H}_2\text{O})$  at  $\sim 25$  eV can be associated with reactive scattering of an energetic proton<sup>74</sup>. There is also a primary threshold energy for

$\text{H}^+(\text{H}_2\text{O})_{n=1-7}$  from PASW, ASW and CI at  $\sim 70 \pm 3$  eV. The only distinct accessible transition at this energy is direct double ionization of the  $2a_1$  level<sup>75, 76</sup>. The production of a two hole state at this level occurs with a relatively small cross section approximately two orders of magnitude smaller than that of single ionization, however, since this state alone is primarily responsible for cluster ion desorption, this experiment is sensitive to it.

Two holes localized on a single water molecule is an unstable condition due to strong hole-hole repulsion. This level however, is not low enough in energy to allow for Auger decay in a gas phase water molecule since the 3<sup>rd</sup> ionization potential is too high. Coupling to nearest neighbor molecules, however, allows alternative mechanisms to switch on, including charge transfer (hole hopping), proton transfer and Intermolecular Coulomb Decay (ICD)<sup>75</sup>. Each of these decay mechanisms leads to the same final state: two positive charges on adjacent water molecules in the lattice.

Cluster production then follows after the initial formation of the  $2a_1^{-2}$  state in the near surface region by a series of steps. The decay of the initial two hole state can proceed by via several different pathways, the relative importance of which is determined by relative timescales. The two hole state can draw an electron from an adjacent molecule or a two-site Auger decay mechanism has been proposed known as ICD. Both of these channels result in two singly ionized water molecules in close proximity. Once this charge separation has occurred, the ionized molecules subsequently undergo unimolecular dissociation resulting in only protonated clusters<sup>77</sup>. Alternatively, the two hole state can decay by fast, possibly ultrafast, dissociation, breaking into  $\text{H}^+$  and  $\text{OH}^+$  fragments. The proton then will become incorporated into an  $\text{H}_3\text{O}^+$  moiety due to the strong proton affinity of water. The  $\text{OH}^+$  fragment has a higher IP than water, and

therefore will quickly transfer its charge to the nearest molecule to it. These processes are indistinguishable in this experiment since they each result in protonated water species and a neutral OH fragment which we do not detect. However, we note that recent x-ray emission (XES) and photoemission spectroscopy (PES) and quantum molecular dynamics simulations provide evidence supporting ultrafast dissociation of core-ionized water in crystalline ice<sup>78</sup>. The shift of the  $1b_1$  level towards a lower binding energy is indicative that the internal O-H bonds have increased in length, becoming less bonding. The simulations indicate that both internal O-H bonds dissociate, with one ultimately reforming creating  $O(1s)^{-1}H$  and  $H_3O^+$ .

#### 3.4.5 Cluster Growth and Ejection

The electron flux dependence of the cluster yield is linear, indicating a single electron impact event. This flux dependence, together with the threshold data and similar kinetic energy distributions of all the clusters (see Fig. 3.4) can be used to model the distributions observed in Figure 3.1. If the two neighboring ions remain localized (within 1 - 2 nm of each other) for approximately 100 fs, a cluster ion, whose kinetic energy is determined by the potential of the localized charges, can be produced. Water molecules surrounding these neighboring charges quickly screen them by donating electron density, polarizing or reorienting their dipole moments toward the charge. This screening effect is identical to the process of forming an ion-dipole bond in a cluster. The binding of successive water molecules to a proton is reflected in the hydration enthalpies. Consequently, the formation of the cluster is a competition between the tendency to form the ion-dipole bond versus the attraction to the nascent lattice site. The energy required

to nucleate a cluster, therefore, comes from the energy needed to create the hole, not from the energy of any impulsive collisional force from hot proton ejection from the initial excitation site or reactive scattering. The reorganization of electron density around the positive nucleus of the cluster forms the bonds of the cluster and detach the neighboring waters from the lattice. Bond formation to the ion is more exothermic than the detachment from neighboring water molecules is endothermic. The excess enthalpy must then go into internal energy modes of the cluster or dissipate into the phonon bath of the ice. Plotted in Figure 3.9 is the measured intensity of clusters detected ( $n = 2 - 9$ ). The dominant force governing the cluster growth is the formation of ion-dipole bonds as a result of dielectric hole screening. These intensities can be modeled approximately as

$$I(n) \propto \exp[ - E_H * n / E_n ]$$

Where  $E_H = 0.25$  eV is the average binding energy per hydrogen bond in ice and  $E_n$  is the hydration enthalpy of the  $n^{\text{th}}$  water molecule in the cluster of size  $n$ <sup>79</sup>.

When the double ionization event occurs in the near surface region, the portion of the lattice nearest the surface will be the easiest to detach. The energy of hole-hole repulsion of the nearby charges is essentially purely Coulombic, and as such is very long range. A repulsive potential energy of about 5 eV, corresponding to the measured average kinetic energy of the clusters, is achieved at a distance of 3 Å. This is very close to the average O-O distance in ice for nearest neighbors. This energy is not, however, imparted to the cluster immediately (i.e. not impulsive) but rather has a shallow sloped repulsive curve. Figure 3.10 shows a plot of the Coulomb repulsion between two point charges over distance. The left vertical axis shows the potential energy in electron volts. The right axis shows the kinetic energy of the fragment cluster relative to the initial

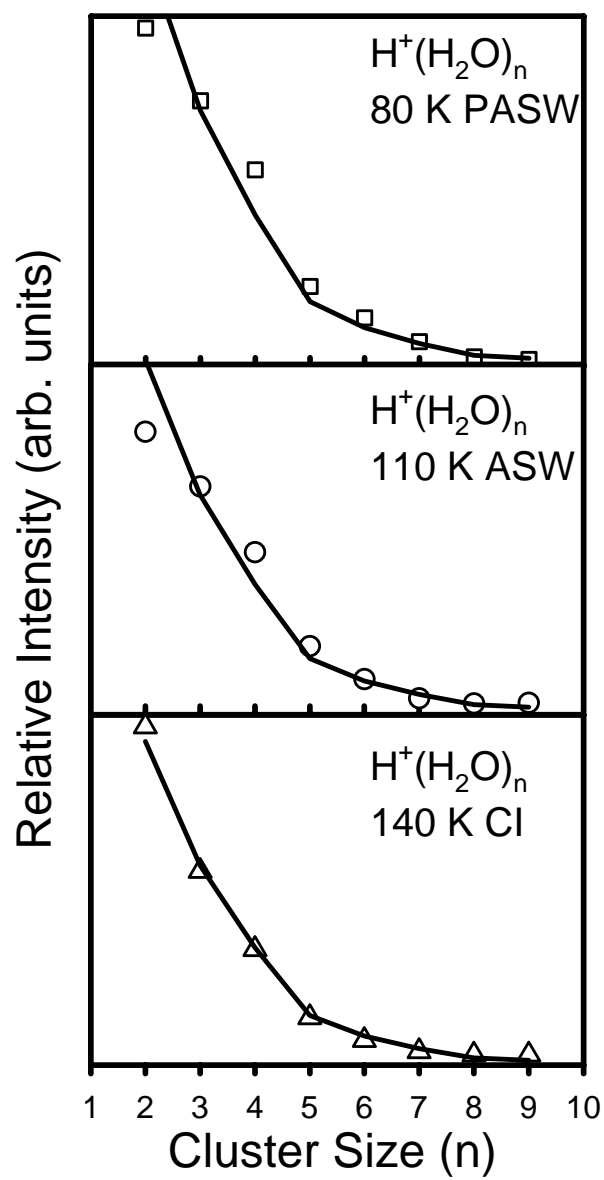


Figure 3.9 Model fit to cluster distribution

separation of about 3 angstroms. Only about 1 eV of repulsive energy is imparted to the expelled cluster in the first angstrom of travel. Beyond this, the cluster will surely have become fully formed and all attachments to the surface will be broken. The remaining acceleration happens slowly, as the cluster moves off to infinity. Therefore, the majority of the repulsive energy imparted to the cluster is not gained until after separation, and is not available yet at the time and place of the cluster formation event. This final push must then be independent of cluster size.

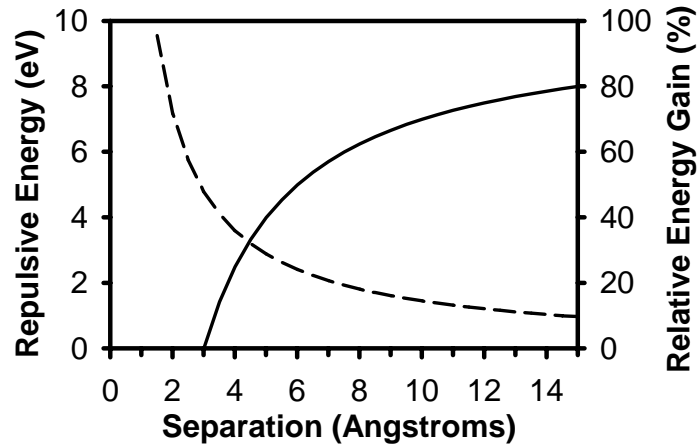


Figure 3.10 Coulomb repulsion between two point charges

### 3.4.6 Temperature Effects

The temperature dependence of the  $\text{H}_2^+$  and cluster ions shown in Figure 3.5 can be understood in terms of excited-state lifetimes, hole-localization probabilities, screening effects and local bonding geometries. ESD is an ultra-fast probe (on the timescale of 10 - 100 fs) which provides the ability to probe the local bonding geometry of the surface molecules with a high degree of sensitivity. Protons are formed mainly from the dangling bonds at the surface that point into the vacuum or water molecules within the first water bilayer with a direct line of sight to the vacuum. These dangling bonds are not fully coordinated, thus, the holes produced in these surface molecules are localized. At low temperature, the overall hole delocalization or hole hopping efficiency is lowered due to reduced coupling to neighboring water molecules leading to a high proton yield. At low growth temperatures, the water molecules are randomly oriented and the hydrogens of the surface water molecules may be pointed along the ice surface or towards the bulk ice. The result is a low proton yield for PASW compared to CI. As the temperature increases, the surface water molecules can break hydrogen bonds, leading towards a greater number of dangling bonds and a perturbed gas-phase like interaction potential for the surface molecules. In fact, there is a return of the atomic  $p_z$ -character to the wavefunctions of terminal water molecules with reduced hydrogen bonding interactions.

It is well established that a narrow bandwidth is correlated with efficient hole-hole localization<sup>80</sup>. If the effective hole-hole interaction energy,  $U_e$ , is greater than the bandwidth, then hole localization will occur. According to the photoemission data shown

in Figure 3.7, the “bandwidths” of ice are rather narrow (less than a few eV) and thus ice is a very good system for hole-localization. Typically, the desorption yield scales as  $Y \sim e^{-\tau_c \Gamma}$  where the bandwidth  $\Gamma$  and  $\tau_c$  is the critical lifetime. Note that  $\tau_c$  depends upon the coupling strengths and  $\Gamma$  is the degree of hydrogen bonding. As the temperature is increased, reduced coupling results in narrower bands and a longer lifetime. Configurations such as  $(3a_1)^{-1}(1b_1)^{-1}(4a_1)^1$  and  $(3a_1)^{-2}(4a_1)^1$  are particularly sensitive to temperature and produce protons with kinetic energies ranging from 0 - 4 eV. The temperature effect on proton and  $H_2^+$  yields can be understood primarily in terms of increased contributions from these levels due to increased excited state lifetimes. The velocity distributions shown in Figure 3.4, the photoemission data in Figure 3.7 and in previous work which reported the appearance of ‘slow’ protons at higher temperatures<sup>32</sup> supports this contention. The mobility of defects and reorientation of the surface molecules also lead to higher proton and  $H_2^+$  yields with increasing temperature.

When a single or multi-hole state is produced in sub-surface water molecules, holes may ‘hop’ to neighboring molecules through a hydrogen bond, forming a trapped hydronium ion. As mentioned previously, two holes in close proximity to one another cause a Coulomb explosion resulting in the desorption of cluster ions  $H^+(H_2O)_{n=1-8}$ , where  $n$  depends on the local geometry of the surrounding water molecules. As is shown in Figure 3.5, each cluster ion shows a strong decrease with temperature up to about 120 K, where a plateau is reached. Above 160 K the ice begins to sublime in the vacuum. The efficiency of  $2a_1^{-2}$  decay into two-localized holes or a  $H_3O^+:H_2O^+—OH$  configuration is mediated by the through-bond coupling of the H-bond network. Stronger coupling occurs at lower temperatures where bands involved in H-bonding have broader dispersion



and are more delocalized over the neighbors. This coupling effect is in direct proportion to the core-hole screening strength and stronger coupling increases the efficiency of core hole hopping to a neighboring water molecule.

The Debye-Hückel screening coefficient varies with temperature as  $T^{-1/2}$  and comparison of this temperature and distance dependent screening strength with the cluster ion yield as a function of temperature is shown in Figure 3.11 where the temperature dependence for a chosen representative water cluster ( $n = 3$ , ■) is compared to the temperature dependence of the Debye-Hückel screening factor (gray line). The efficiency of charge screening modulates cluster production due to both hole localization/hopping competition as well as cluster binding efficacy. The strength of screening directly correlates to hole localization, since this represents the coupling of neighboring water molecules to the core hole at its origin. As the screening strength drops, and temperature increases, hole hopping becomes less efficient. Cluster ejection from the ice surface requires hole transfer from one molecule in a two-hole state to create two adjacent holes, so detection of clusters is commensurate. Meanwhile, as stated above, hole screening occurs by the strengthening of ion-dipole bonds which form the clusters. At lower temperatures, this increases the efficacy of cluster bond formation from the core-hole creation.

At low temperatures ( $< 120$  K) the correlation is strong. At about 120 K the correlation begins to deviate. This is the thermal energy required for D-defect mobility, molecular rotation in the lattice and the lattice relaxation<sup>81</sup>. Water clusters and molecules may undergo surface diffusion between 80 – 120 K with the onset possibly<sup>82</sup> as low as 60 K. Thus, as the temperature increases, the surface can also anneal and crystallize<sup>32, 49</sup>.

Although bond mediated core hole screening continues to decrease above 120 K, thermal movement of the ice makes lattice relaxation, hole self-trapping and solvation possible. This prevents the yields from continuing to drop since these mechanisms for distributing charges can now contribute to cluster formation. This acts to sustain cluster production up to the desorption temperature of 160 K.

In summary, the temperature effects provide insight into: 1.) hole localization at the surface of the ice correlated to the narrowing of the bandwidth, 2.) hole delocalization in subsurface water molecules (in the first 3-4 layers) and 3.) defect mobility and reorientation of surface molecules.

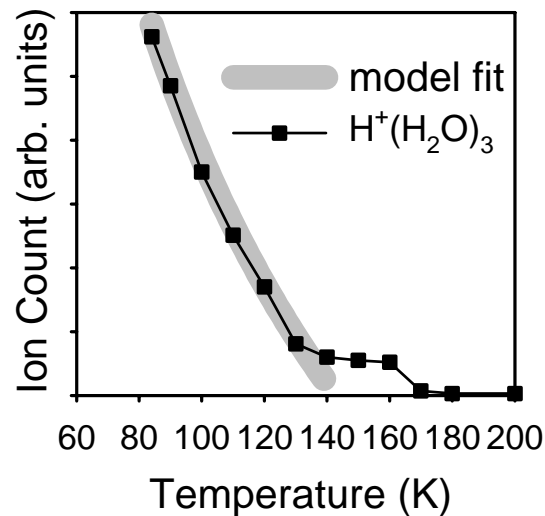


Figure 3.11 Temperature dependence of Debye-Huckel screening distance

## CHAPTER 4

### INTERACTION OF HCl WITH ICE SURFACES

#### 4.1 Overview

The interaction and autoionization of HCl on low-temperature (80 - 140 K) water ice surfaces has been studied using low-energy (5 – 500 eV) electron-stimulated desorption (ESD) and temperature programmed desorption (TPD). There is an enormous reduction of the proton and  $\text{H}_2^+$  ESD yields and a concomitant increase in the protonated cluster signals due to the presence of sub-monolayer quantities of HCl. The results indicates non-activated autoionization of HCl occurs at surface at temperatures as low as 80 K; well below those typical of polar stratospheric cloud particles. The autoionization of HCl forms ion-pair states that lead to disorder, reduced numbers of dangling bonds at the surface and increased hole-localization. The latter results in the formation of clusters primarily by increasing the contribution of the two-hole final states necessary for cluster ion formation. The uptake and facile autoionization of HCl is further supported by TPD studies which show that for HCl doses of  $< \sim 0.8 \pm 0.2$  ML, desorption of HCl occurs at about 150 K and is commensurate with the desorption and removal of the multilayer ice. Adsorption of molecular HCl does occur at temperatures below 120 K but the dose at which this occurs is strongly dependent on the annealing history of the ice. The activation energy ( $E_a$ ) for second order desorption of HCl initially

in the ionized state is  $43 \pm 2$  kJ/mole, i.e. the zero order activation energy for ice desorption.

## 4.2 Experimental Details

The experimental apparatus has been described in Chapter 2, however there are a few modifications that have been made to improve the measurements and facilitate the study of HCl on ice surfaces. Briefly, the system is composed of an ultra-high vacuum (UHV) chamber with a typical base pressure of  $2 \times 10^{-10}$  torr. The oxidized zirconia sample substrate is attached to a rotatable cryohead allowing a temperature range of 80 – 600 K and the ability of the sample to rotate to face any ports in the ultra-high vacuum chamber. The temperature was controlled via a computer and feedback loop for TPD measurements as well as controlling the morphology of the ice sample. The pulsed electron gun was at a 45 degree incident angle to the sample substrate and the electron energy could be varied from 5 – 250 eV. The UHV chamber was also equipped with a quadrupole mass spectrometer used for the detection of neutral species as well as a time-of-flight mass spectrometer used to detect ions. The configuration of the electron gun, time-of-flight (TOF) mass spectrometer and sample was designed to allow field free measurements to be taken with the TOF at a 90 degree angle to the sample (see Figure 2.1). A 100 V extraction field on the TOF was typically used to collect the desorbing cations except when recording velocity distribution measurements where field free conditions were implemented.

A carefully designed dosing system was fabricated for the investigation of HCl and ice surfaces. Precautions were taken to eliminate any effects of co-dosing HCl with water since this may lead to the dosing of ionized species. Therefore, the chamber was equipped with two completely separate dosing lines terminated in leak valves with directed dosing tubes. The dosing lines were thoroughly baked and equipped with a liquid nitrogen trap. The HCl dosing line used a directed glass dosing tube and was purged to passivate the surface. Mass spectrometer studies during dosing indicate the HCl to be contaminant free. The water samples ( $\text{H}_2\text{O}$  and  $\text{D}_2\text{O}$ ) were purified by several freeze-pump-thaw cycles prior to dosing and the ice samples were vapor dosed at controlled temperatures designed to specifically grow porous amorphous solid water (PASW – 80 K), amorphous solid water (ASW – 110 K), or crystalline ice (CI – 140 K).

A minimum of 40 ML was found to be sufficient to decouple the surface of the ice from the substrate, and all samples were > 50 ML to ensure the measurements were not affected by the substrate. HCl coverages were determined by measuring the pressure change in the chamber during dosing corrected with an enhancement factor of 100 to account for the directed dosing. This is an upper limit to the amount of HCl and assumes a unit sticking probability. At low temperatures the HCl sticking probability is close to unity however at higher temperatures (specifically those samples dosed at 140 K) the coverage of HCl is most likely lower than calculated.

### 4.3 Time-of-Flight (TOF) Spectra of HCl Dosed Ice Surfaces

The cations produced and desorbed during 250 eV electron impact of pristine ice are depicted Figure 4.1 for pure (solid line, gray area) and HCl (dashed line, white area) dosed (A) PASW, (B) ASW, and (C) CI. The proton and  $\text{H}_2^+$  signals are shown in the top panel with the corresponding cluster signals in the bottom panel. A detailed description of the cation yields from pristine ice can be found in Chapter 3. Briefly, the cation yield is dominated by  $\text{H}^+$  with a much smaller yield of  $\text{H}_2^+$ . The  $\text{H}^+$  and  $\text{H}_2^+$  yields increase with increasing dosing temperature with ratios of 1:2:3 (PASW:ASW:CI) for  $\text{H}^+$  and 1:1:1.5 for  $\text{H}_2^+$ . There is also a very reproducible protonated cluster ion signal. The cluster yield from PASW is typically 5-6 times larger than CI, and the ASW cluster yield is about 2-3 times larger than CI<sup>83</sup>. A very interesting and dramatic change in the ion yields occurs due to the presence of small amounts of HCl. This can be seen in Figure 4.1 where the dashed lines represent the ESD yields after a dose of  $\sim 0.1$  ML of HCl. The CI shows the most dramatic increase in the cluster yield, followed by the annealed ASW and PASW ice films. In contrast to the cluster yields, the  $\text{H}^+$  and  $\text{H}_2^+$  yields significantly decrease upon adsorption of HCl.

Dosing PASW with small amounts of HCl resulted in a cluster yield approximately 130% that of the pristine PASW. A greater increase in the cluster yield is observed when ASW is dosed with HCl. Dosing HCl on ASW increases the cluster yield by 3-5 times (Figure 4.1), bringing the HCl dosed ASW yield approximately to that of bare PASW. The largest relative increase in the cluster yield is observed for HCl on CI. Specifically, the first and second cluster signals were larger by over a factor of five and

eight times, respectively, with the presence of  $\sim 0.3$  ML HCl on  $\text{H}_2\text{O}$  at 140 K. This sample also showed the largest decrease in the  $\text{H}_2^+$  signal, decreasing over 80%. Although the adsorption of HCl also causes a substantial decrease in the proton signal, this decrease could not be quantified due to the large proton signal from pure ice samples saturating the detector.

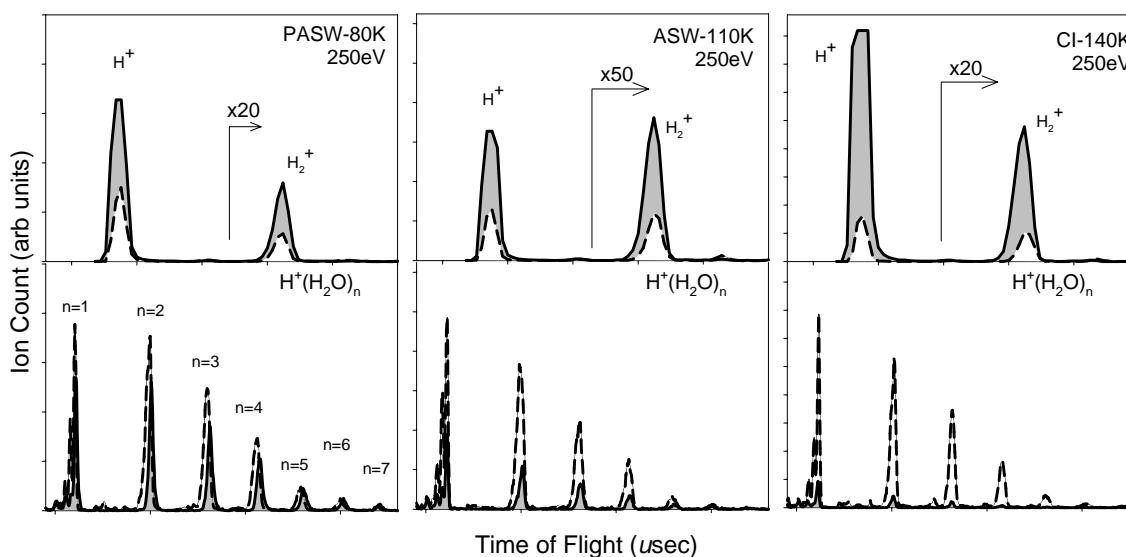


Figure 4.1 Cation yield of pristine and HCl dosed ice surfaces

When CI was initially grown at 140 K, then lowered to 80 K for HCl dosing, and finally raised back to 140 K prior to irradiation, approximately the same increase was seen in the clusters with the same HCl dose. It is important to note that the CI sample dosed and irradiated at 80 K also showed an increase in the cluster ion yield, although the change was not as large as with dosing at higher temperatures. The protonated dimer

yield increased the greatest amount in all samples and showed the most extensive isotope exchange using HCl and D<sub>2</sub>O (see section 4.5).

#### 4.4 ESD Cation Yield as a Function of HCl coverage

Figure 4.2 shows the relative increase in cluster yield as a function of HCl coverage. The filled symbols correspond to  $\text{H}^+(\text{H}_2\text{O})$ , and the dimer ( $\text{H}^+(\text{H}_2\text{O})_2$ ) is shown as open symbols. CI, ASW, and PASW samples are represented by circles, squares, and triangles in panels 4.2.A, 4.2.B, and 4.2.C, respectively. Dosing each phase of ice at different temperatures provided a unique response to increasing amounts of HCl. CI dosed at 140 K (circles) shows the largest relative change. The smallest increase is the PASW (triangles) dosed at 80 K, with the clusters approaching twice the value of the bare ice sample. While this relative increase is the smallest of all samples, it is important to note the PASW had the highest overall cluster yields. The cluster yield from HCl-ASW (squares) dosed at 110 K is 3-4 times the value of the pure ice, reaching this value at ~ 0.5 ML HCl coverage. Similar to the ASW sample, CI at 140 K also reaches an upper limit to the clusters between 0.5-0.6 ML in the low-coverage regime studied. After an initial dose of HCl on PASW, the  $\text{H}_2^+$  yield dropped ~30%, decreasing by ~80% after ~0.75 ML HCl. The proton yield also decreased significantly with HCl dosing.



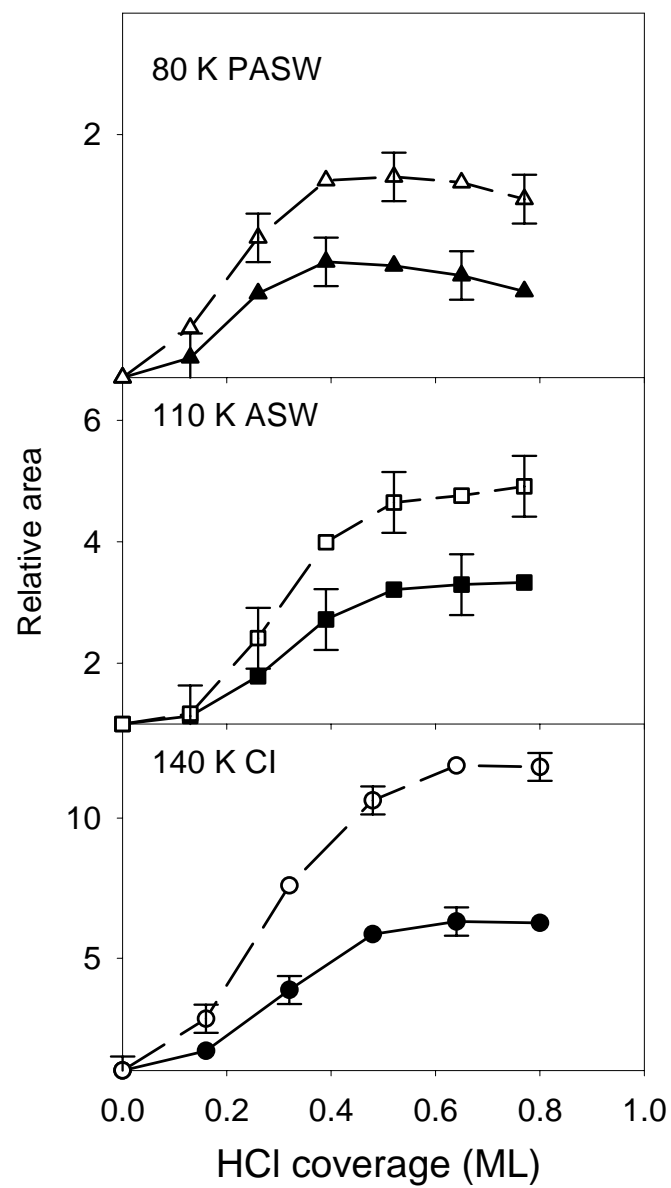


Figure 4.2 Cation yield as a function of HCl coverage

## 4.5 Isotope Exchange

D<sub>2</sub>O was used to study the isotope exchange with HCl in the desorbing clusters to probe for autoionization. The exchange in the dimer ion D<sup>+</sup>(D<sub>2</sub>O)<sub>2</sub> is the most extensive so the discussion will concentrate on this observation. Analysis of the relative abundances of isomers composing the cluster ion yields illustrates the isotope exchange is not statistical, most noticeably in the PASW and ASW samples. Specifically, these low temperature samples show an enhancement of the protonated cluster (H<sup>+</sup>(D<sub>2</sub>O)<sub>n</sub>) that is larger than what is predicted by simply a statistical distribution. The isotopic distribution for the CI sample shows the relative ratio of the purely deuterated to the singly protonated cluster yield is closer to a statistical distribution. However, the measured yields of the clusters with more extensive proton incorporation (2-3 hydrogen atoms) are smaller than predicted by this distribution.

Figure 4.3 shows the isotope exchange seen in the dimer ion (D<sup>+</sup>(D<sub>2</sub>O)<sub>2</sub>, mass 42 amu) from CI and ASW. The thin solid or dashed lines are the Gaussian curves for each mass, the thick solid line is the sum of Gaussian fits which fit the data points (solid triangles – pure ASW, solid circles – HCl dosed ASW) accurately. These TOF spectra are typical of samples from HCl dosed on D<sub>2</sub>O, with other samples showing slight variation in the overall degree of isotopic mixing. The solid and dashed thin lines show the Gaussian fits for each mass, the data points for the pure ice and HCl dosed ice are shown as the triangles and circles, respectively, and the line shows the overall fit to the data. As previously stated, special care was taken to separate the dosing of water and

HCl to rule out any co-dosing. Isotope exchange was also observed at 80 K with hydrogen substituted clusters from HCl dosed PASW.

With a low dose of HCl on PASW ( $D_2O$ ) (not shown), the overall cluster yield of  $n = 2$  increases by 20% and 70% with successive HCl dosing, however, mass 42 ( $D^+(D_2O)_2$ ) actually decreases. The protonated  $n = 2$  cluster ( $H^+(D_2O)_2$ , mass 41), which is absent from the pure ice spectra, grows to 33% of the value of mass 42 with  $\sim 0.1$  ML HCl and is of equal area with  $\sim 0.65$  ML HCl.

Similar to PASW, isotope exchange is evident when dosing ASW samples at 85, 90 and 110 K (Figure 4.3B). When the ASW sample was dosed at 85 and 90 K, singly hydrogen substituted clusters ( $H^+(D_2O)_2$ ) were enhanced by a factor of over four and the doubly substituted hydrogen clusters ( $H^+(H_2O)(D_2O)$ ) increased by a factor of ten with  $\sim 0.75$  ML HCl. Dosing HCl on ASW at 110 K shows an increase comparable to the lower temperature dosing however the isotope exchange is less extensive in the doubly hydrogen substituted clusters ( $H^+(H_2O)$  and  $H^+(H_2O)(D_2O)$ ) when dosing at 110 K. This may indicate that the proton forms a contact ion pair at the lower temperature and is still available at the surface. However, at higher temperatures where surface diffusion and defect mobility start to turn on<sup>82</sup>, the proton is able to diffuse through the ice and is less likely to be found at the surface.

The isotope exchange is most drastic for crystalline ice, with certain isotopes growing 18x larger with HCl dosing (Figure 4.3A). This large increase is partially due to the initially low cluster yield from CI but demonstrates the importance of the incorporation of the proton into the cluster signals. The singly hydrogen substituted cluster shows the largest relative increase for both  $n = 1$  and  $n = 2$  water clusters, growing

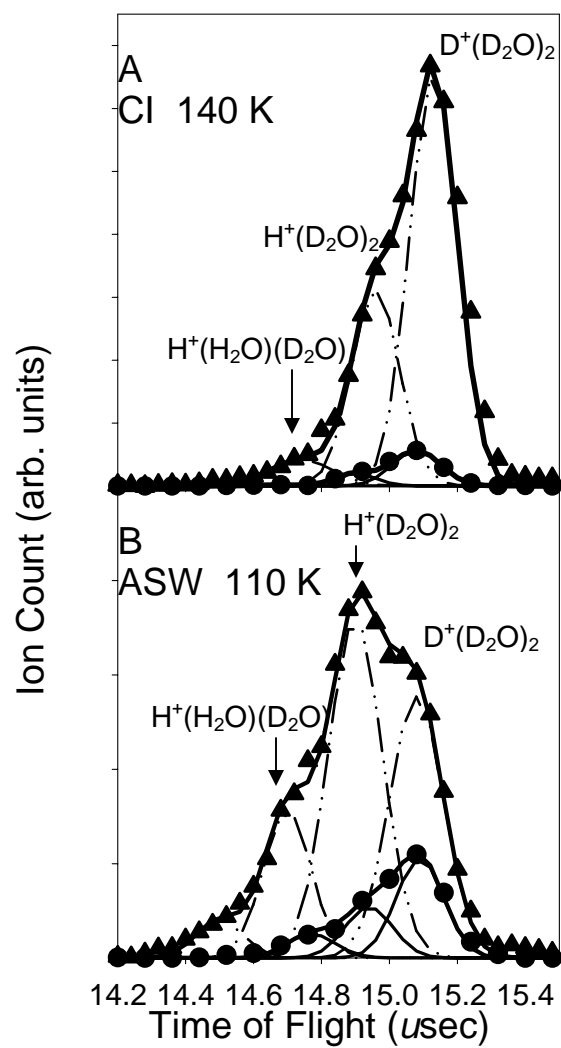


Figure 4.3 Isotope exchange in dimer cluster

~ 10x with ~ 0.4 ML HCl further increasing to ~ 18x with ~ 0.8 ML HCl. The purely deuterated clusters also increase in response to the HCl dosing, growing over 5x and 8x with ~ 0.4 ML and ~ 0.8 ML, respectively. While the percentage increase is largest for the singly substituted clusters, these H-containing clusters comprise only ~ 30% of the total cluster yield for crystalline ice. The resulting ratio of the purely deuterated and singly substituted clusters can be approximated with a statistical distribution of the D and H atoms, however this fails to correctly predict the overall yield as it overestimates the clusters with more extensive hydrogen incorporation.

#### **4.6 Velocity Distribution of Protons with and Without Adsorbed HCl**

Due to the large proton yield, its velocity distribution could be measured under field-free conditions (no extraction potential). The TOF taken under these field free conditions can be converted into a kinetic energy distribution by using the Jacobian transformation  $I(E) = I(t)t^3/(mL^2)$  where  $I(t)$  is the intensity as a function of time ( $t$ ),  $m$  corresponds to the mass of the ion, and  $L$  is the length of the flight path traveled by the ion. The velocity distributions of the proton from CI and PASW are shown in Figure 4.4, the solid squares are the Jacobian transformation of the data for pure ice samples and the open circles are for HCl dosed ices. The dotted and dashed lines in Figure 4.4A (CI) represent the Gaussian curves fit to the data with the sum shown as a solid line. The solid and dashed lines in 4.4B (PASW) are the fits to the data. The Gaussian curves describe the data reasonably well. The distribution from CI can be represented by two Gaussian curves with peak kinetic energies of ~ 4 eV and ~ 8 eV, indicating that at least two

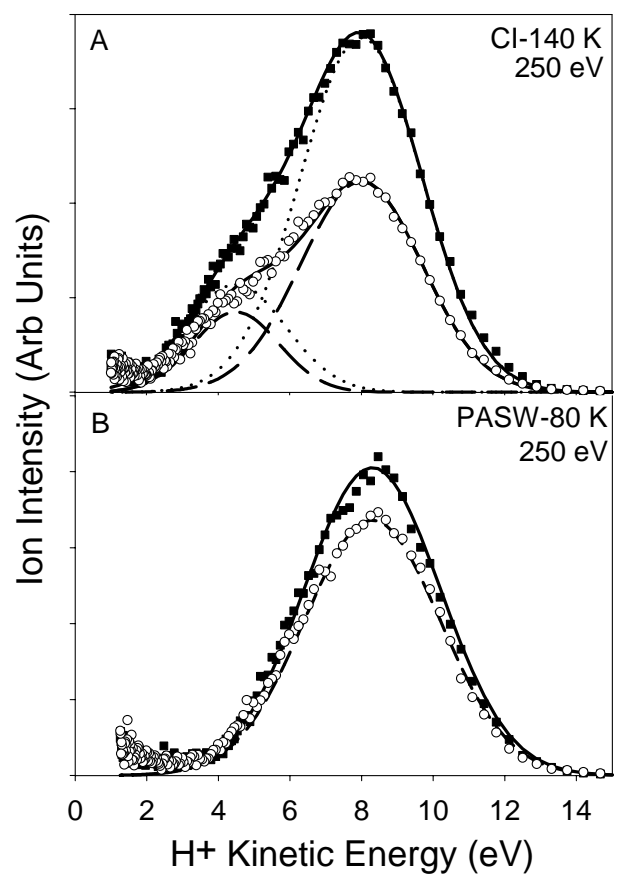


Figure 4.4 Velocity distributions of protons with and without adsorbed HCl

channels are responsible for proton production and desorption. At lower temperatures, only the first spectrum recorded shows a small contribution from the lower energy channel (not shown), most likely the result of dangling bonds that are efficiently removed during the first electron pulses. The resulting spectrum is fit with one Gaussian curve centered at  $\sim 8$  eV. The addition of HCl reduces the overall proton yield for both temperatures, with the CI showing the greatest decrease upon HCl dosing. Note that there is no shift in the kinetic energies of the protons with HCl dosing, indicating that the surface is not charging.

#### **4.7 Temperature Programmed Desorption (TPD) of HCl: Ice at Several Growth Temperatures**

TPD was performed after ESD-TOF measurements as well as on non-irradiated samples to ensure the irradiation was not influencing the observed ionization of HCl. Figure 4.5A is a typical TPD trace from HCl dosed ice, the dashed line corresponds to water desorption (divided by 5 due to intensity) and HCl desorption is shown as the solid line. Although Figure 4.5A shows a sample dosed and maintained at 150 K, all of our low-dose ESD samples yielded this same TPD spectra, regardless of dosing temperature. All of the TPD spectra for the corresponding ESD-TOF spectra shown have only one HCl TPD peak which is coincident with the water desorption peak. As discussed later in this paper, we interpret this as a strong indication of HCl ionization on the ice surface.

Slightly higher doses of HCl were also used in TPD studies to examine the effect of the dosing temperature and ice phase. Although this is not an in-depth investigation of HCl TPD from ice (which has been done previously<sup>21, 25-28, 84, 85</sup>), it provides useful insight into the interaction of acid on the ice surface. Figure 4.5 shows the temperature programmed desorption spectra of HCl dosed on ice at (A) 150 K, (B) 110 K, and (C) 80 K on CI, ASW, and PASW, respectively. The dashed line is the water desorption (divided by 5 for comparison) and the solid line is the HCl desorption. As shown in Figure 4.5, there are three main desorption features that occur under various dosing conditions for HCl fluxes greater than those used in the ESD experiments ( $> \sim 0.8$  ML depending on dosing conditions). The first is the feature (I) which desorbs in coincidence with the water desorption. The second feature (II) is a shoulder (non-resolved peak) which can start between 110 K and 130 K depending on HCl dosing temperature and leads into the first feature. The lowest temperature feature (III) occurs when dosing HCl below 110 K. This final low temperature feature has the least amount of interaction with the ice surface, while the second shoulder feature is more strongly tied to the ice surface yet still able to desorb before water. With this technique we are not able to probe the exact stoichiometry of the interaction however we can gain insight into the strengths of the interactions involved. The doses at which these additional features were measured were greater than those used for the ESD studies.



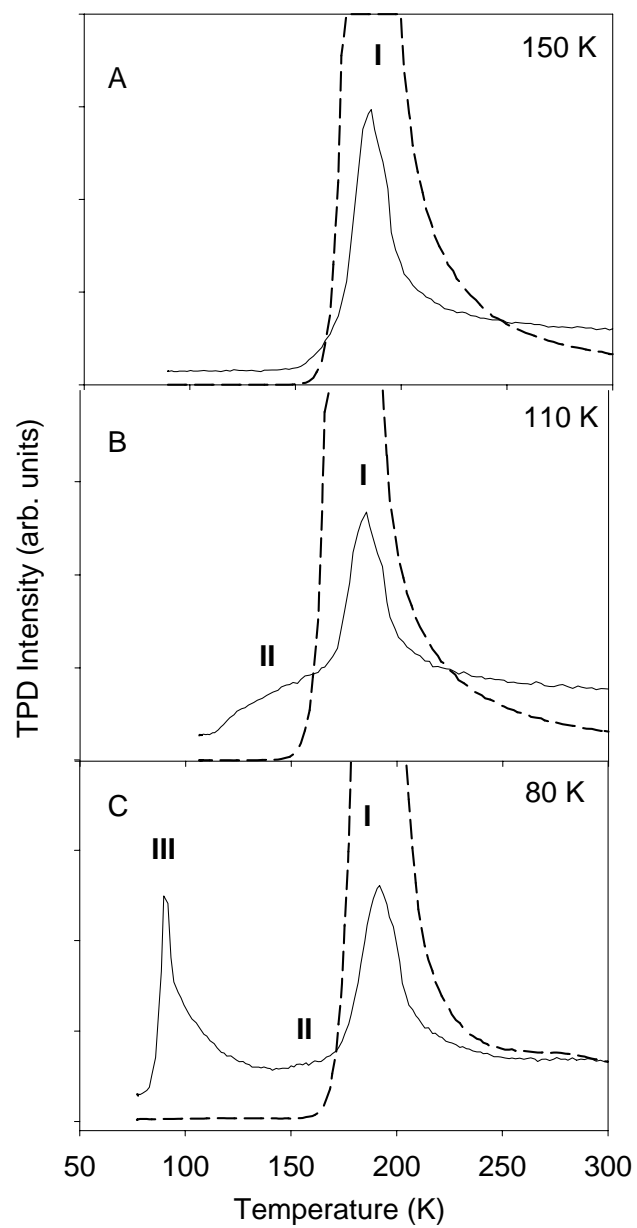


Figure 4.5 TPD of HCl dosed ice from CI, ASW, and PASW

## 4.8 Cation ESD Mechanism

Here we provide a brief review of the electronic structure of condensed phase water and the excited states leading to proton desorption. A more detailed description of the electronic structure of water can be found in Section 3.4.1 and previously published work<sup>32, 83</sup>. Calculations and photoemission data show the electronic structure of condensed ice retain much of their gas-phase character with some broadening and minor shifting of the energy levels. The largest change in the condensed phase occurs in the  $a_1$  levels which are significantly broadened, (compared to the  $1b_1$  and  $1b_2$  bands), and are most affected by hydrogen bonding. Specifically, the unoccupied  $4a_1$  orbital is in the band gap, spatially extended, and mixed with the  $2b_1$  level. As previously discussed, levels with  $a_1$  character should be sensitive to the local bonding environment of the water molecule<sup>86</sup>.

### 4.8.1 Proton Desorption Mechanism

There are at least four two-hole or two-hole one electron configurations known to produce protons with kinetic energies ranging from 0 to greater than 7 eV kinetic energy (see Figure 3.8)<sup>32, 40, 45</sup>. These two-hole and two-hole one-electron excited states involve bands of  $a_1$  symmetry, which are involved in hydrogen bonding. This contribution of the levels which participate in hydrogen bonding cause the characteristics of the excited states to be affected by the local hydrogen bonding environment of the excited water molecules. The dependence of the excited state lifetimes on the local hydrogen bonding

environment allows us to use the proton yields to gather information about the local geometry and dynamic response of the ice surface.

The linear dependence of the proton yield on dose as well as the threshold energy indicated that low energy ( $\sim 4$  eV) proton desorption is the result of 2-hole states occurring at the surface of the ice and has been assigned to  $(3a_1)^{-2}(4a_1)^1$  and  $(3a_1)^{-1}(1b_1)^{-1}(4a_1)^1$  final states of water. The dangling bonds at the ice surface are likely to be the main source of these low energy protons. There is a secondary threshold  $\sim 40$  eV which may correspond to the  $(3a_1)^{-2}(4a_1)^1$ ,  $(3a_1)^{-1}(1b_1)^{-1}(4a_1)^1$  and  $(1b_1)^{-2}(4a_1)^1$  states of water producing protons with kinetic energy up to 7 eV. Energetic or ‘fast’ protons ( $> 7$  eV) can also be produced from  $(2a_1)^{-2}$  at incident electron energies of  $> 70$  eV.

The temperature dependence of the proton yield gives insight into the local configuration of the surface of the ice and the dangling bonds responsible for proton production. At low dosing temperatures, the random orientation of the surface water molecules leads to a low proton yield for PASW compared to CI most likely because the proton undergoes reactive scattering across the ice surface or into the bulk<sup>50</sup>. As the temperature increases, the mobility of the surface water molecules increases as the molecules have sufficient energy to rotate and start to diffuse<sup>82</sup>. This reduces their hydrogen bonding interaction and is supported by the photoemission data showing the narrowing of the  $a_1$  bands from condensed to gas phase leading to longer excited state lifetimes and the increased probability for proton emission<sup>32, 83</sup>.

#### 4.8.2 $\text{H}_2^+$ Desorption Mechanism

$\text{H}_2^+$  desorption has similar threshold values compared to  $\text{H}^+$  however the yields are much less. There are several possible production pathways for  $\text{H}_2^+$ . Although the branching ratio is small, the two-hole and two-hole one-electron states responsible for proton desorption can also decay to form  $\text{H}_2^+$ . This has been observed in the time correlate dissociation of doubly ionized states of water, most likely through a dissociative triplet state<sup>67</sup>. With the 250 eV electrons used in these experiments, the partial cross section for proton production is greater than 200 times<sup>64</sup> that of  $\text{H}_2^+$ . Photoionization near the O  $1s \rightarrow 2b_2$  resonance<sup>65</sup> was reported to produce  $\text{H}_2^+$ . The absorption of four photons to produce  $\text{H}_2^+$  ( $X^1\Sigma_g^+$ ) was also reported in a recent multiphoton ionization study<sup>66</sup>. The  $\text{H}_2^+$  yield observed from the ice samples in this work compared to gas phase studies indicate many body interactions may play a role in its production. Orientational D-defect configurations present in ice as a dimer arrangement can produce  $\text{H}_2^+$  from a doubly ionized water molecule. Reactive scattering may be a source of  $\text{H}_2^+$ , although there are solvation and polarization forces that present a barrier to desorption. The linear flux dependence of the production of  $\text{H}_2^+$  supports both a single electron impact event and a direct stripping of a proton at the surface. Further discussion of this mechanism can be found in Section 3.4.3.

#### 4.8.3 Cluster Production Mechanism

The mechanism for cluster ion desorption involves the production of two holes and a Coulomb explosion resulting from these holes in neighboring water molecules<sup>86</sup>. A detailed description of this model can be in section 3.4.4. Briefly, the weak threshold  $\sim 25$  eV for  $\text{H}^+(\text{H}_2\text{O})$  is most likely due to the reactive scattering of an energetic proton<sup>74</sup>. The primary 70 eV threshold for clusters with 1-7 water molecules corresponds to the  $2a_1^{-2}$  state. Coupling of this water molecule in its excited state to a neighboring water molecule leads to the final state of one positive charge on each of the two water molecules, most likely with an  $\text{OH}^+ \dots \text{H}^+(\text{H}_2\text{O})$  configuration. This can occur either through either ICD or ultrafast dissociation. The surrounding water molecules respond to the charges by reorienting in an attempt to solvate the charges, and finally the unstable configuration undergoes a Coulomb explosion resulting in desorption of a protonated cluster.

The temperature – phase dependence of the cluster ion yield provides insight into the local hydrogen bonding in the terminal water layers. The cation yield from the ice surface is characteristic of the highest annealing temperature of the ice. While the proton yield reflects the behavior of the surface molecules in direct line of sight to the vacuum, the clusters reflect the behavior of the terminal 1-3 water layers. At low dosing temperatures, the water molecules are randomly oriented and there is no long range order. The localization of two holes can cause dissociation and proton transfer (or hole hopping) along the hydrogen bond, forming a hydronium ion. The holes are then localized on neighboring water molecules. Due to the lack of an ordered hydrogen bonding network

in PASW, the holes are less likely to be able to hop to a screening distance (1-2 nm) before a Coulomb explosion occurs. This ‘localized hole hopping,’ where a hole hops to a neighboring water molecule but not far enough to be screened, occurs in the terminal 1-3 water layers of PASW and results in a large cluster yield. As the temperature increases, a more crystalline structure is formed<sup>32, 49</sup> and the holes are more likely to hop further away from each other through the hydrogen bonding network. Increasing the temperature from 80 K (PASW) to 110 K (ASW) increases the ability of the water molecules to rotate and re-arrange towards a minimum energy configuration. This configuration maximizes the number of hydrogen bonds and increases the long range order needed for the holes to hop to a sufficient screening distance before a Coulomb explosion occurs, thus decreasing the cluster yield. CI has the most extensive hydrogen bonding network of the samples studied here and the lowest cluster yield, due to the efficient hole hopping through this network. This temperature dependence takes place before any thermal desorption and provides insight into the orientation and interaction of the terminal water layers as a function of temperature.

#### **4.9 Mechanism of HCl Effects on Cation ESD**

The solvation of the HCl can induce changes in the local crystalline structure of the ice surrounding the ionized species. Coupled quantum mechanics/molecular mechanics (QM/MM) simulations of HCl interacting with ice surfaces shows evidence of rapid ionization and change the water-water bond lengths upon ionization<sup>3, 30</sup>. The change in the bond lengths is correlated with the disruption of the hydrogen bonding.

The large charge of the  $\text{Cl}^-$  ion decreases the bond lengths in the molecules closest to the ion, essentially separating them from the remaining water molecules. This decreases the hole-hopping probability and increases the local excited state lifetimes of the water molecules.

The change induced by the HCl solvation is probed by the increase in ESD yields. The two-hole states produced from irradiation decay in several ways. If there is sufficient hydrogen bonding, one of the holes may hop away and the energy from the excited state lost as phonon (vibrational) excitation and local heating. However, if the hydrogen bonding network is disrupted and the hole cannot efficiently hop to a distance to be screened from the second hole, the resulting Coulomb explosion can produce clusters and cause desorption of these charged clusters. Most likely the HCl increases the local excited state lifetimes of the neighboring two-hole states responsible for cluster desorption by changing the hydrogen bond lengths. The increase in the bond lengths decreases the strength of the hydrogen bond between the water molecules and the probability of hole hopping between those molecules. By measuring the increase in the cluster yield resulting from the lattice disruption and reduced hole hopping ability, we gain useful information regarding water surface response to HCl at low temperatures. The increase in the cluster yield is evidence that even at 80 K, the ice is a dynamic surface and the terminal water molecules can reorient to solvate ions.

The reduction in the  $\text{H}^+$  and  $\text{H}_2^+$  yields upon the addition of HCl also shows the importance of dangling bonds in the solvation and incorporation of HCl into the ice sample. The addition of HCl decreases the proton yield by tying the dangling hydrogen atoms due to the solvation of  $\text{Cl}^-$  forming a solvation shell around the anions. The result

is fewer number of dangling bonds which are available to produce protons. These results also agree with calculations which show that dangling bonds, especially on step and edge sites can play important roles in HCl solvation<sup>3,30</sup>.

#### **4.10 Temperature Programmed Desorption (TPD) Discussion**

There are numerous investigations into the TPD of HCl from ice with a wide range of dosing temperatures, HCl dose, ice phase, and annealing history of the ice<sup>19, 25-28, 85, 87, 88</sup>. Both Harnett et al.<sup>25</sup> and Graham and Roberts<sup>26</sup> measured lower temperature features which were dependent on several factors such as total HCl dose, saturation of the underlying ice film, annealing history, and dosing temperature. Harnett et al.<sup>25</sup> found that HCl dosing below 130 K results in an HCl enriched surface layer that leads to HCl desorption before water desorption and proposed the formation of HCl trihydrate at the surface. Graham and Roberts<sup>26</sup> show a similar feature in their TPD spectrum and attribute this feature to an adsorbed state only occurring after saturation of the water film to form HCl hexahydrate. Sadtchenko<sup>85</sup> explored HCl interaction with thick films and found that the annealing history of the ice played a major role in the HCl desorption profile.

The variety of conditions used in the various investigations highlights the importance of understanding the fundamental interaction of the HCl with the ice surface before adding complications such as hydrate formation and HCl-HCl interactions. TPD measurements were taken as a complimentary probe to our ESD measurements and show that with low HCl concentrations, the HCl is strongly interacting with the water



molecules and is most likely ionized at all temperatures studied. The desorption feature measured after all of our ESD measurements support the ESD observations of an ionized species which influences the local bonding network of the ice. TPD measurements of non-irradiated ice under the same dosing conditions used for the ESD measurements show identical results, an indication that the electron bombardment is not inducing the HCl ionization on the ice surface.

Some useful information can be gleaned from the higher dose TPD experiments. It is clear that the TPD feature labeled (I) in Figure 4.5 is evidence of a very strongly interacting HCl species, intimately tied to the water and most likely ionized. Rising edge analysis of the multilayer water desorption peak gave a zero order activation energy of  $41 \pm 2$  kJ/mol, in agreement with previous studies using TPD<sup>55</sup> and isothermal desorption<sup>89, 90</sup>. The activation energy of the ionized HCl desorption feature (I) was found to be  $43 \pm 2$  kJ/mol using the Polanyi-Wigner equation and assuming second order kinetics with a normal prefactor of  $10^{13}$  ML<sup>-1</sup>sec<sup>-1</sup>. The activation energy of the HCl is close to that of the water from ice most likely because the water desorption/diffusion is controlling the rate at which the ionized species recombine.

The nature of peak (II) in Figure 4.5 suggests some interaction of the HCl in which the HCl molecule is interacting with either the ice phase or the ionized HCl species that seems to remain on the ice surface. The Cl<sup>-</sup> ion is most likely located on or near the surface of the ice when the first molecules are initially ionized<sup>14</sup>. The subsequent incoming HCl molecules then find a different surface than the dangling hydrogen bonds present on the pure ice samples. The HCl molecule can interact with the Cl<sup>-</sup> ion through the proton, forming a Cl<sup>-</sup>...H·Cl complex. It is also possible that this interaction is a

lower hydrate complex  $(\text{HCl})(\text{H}_2\text{O})_n$  where  $n = 1 - 3$ , as suggested by Sadtchenko et al<sup>85</sup>. However, because this HCl desorbs prior to the water, it is more likely the HCl molecule interacting with the  $\text{Cl}^-$  forming a trapped molecule at the surface.

The lowest temperature peak (III) is most likely physisorbed HCl which is only weakly interacting with the surface. This occurs at dosing temperatures below 110 K and is the weakest interaction of HCl with the ice sample. These TPD measurements have shown that the first interaction of HCl with ice forms a strongly interacting and most likely ionized complex, and only at higher doses are subsequent interactions seen. These subsequent interactions can be formation of a hydrated surface species, interaction of the HCl with the ionized  $\text{Cl}^-$  ions, or physisorption on the ice surface.

There are several further TPD experiments that would lead to greater insight into the surface states responsible for producing the observed features, such as investigating the infrared spectra of the ice samples. We are modifying the UHV system to include this tool and provide another complimentary probe to our TPD and ESD measurements. TPD has shown that with the small doses employed in our ESD measurements, the HCl is solvated and desorbs with bulk water.

## CHAPTER 5

### LIQUID JET CHAMBER

#### 5.1 Motivation for Liquid Jet Chamber

Despite their importance, higher temperature interfaces are not well understood. Studying the surfaces of liquids presents difficulties due to the presence of vapor from the evaporation of the liquid. The dense vapor precludes the use of surface sensitive techniques traditionally used to examine interfaces. Impurities are also problematic when studying liquid surfaces as it is difficult to maintain a clean surface.

While the earlier studies presented here involved low-temperature ice surfaces, there is a desire to reach higher temperatures more reminiscent of the stratosphere. Ultra-high vacuum (UHV) studies of the air-ice interface are limited to temperatures below 160 K, when the ice rapidly sublimates due to its high vapor pressure. In order to approach to the complexity of the system, we initially started with the low temperature ice surfaces<sup>45</sup>, providing insight into the interaction of adsorbates with terminal water molecules. This low temperature system provides a knowledge ‘base’ that we can use and apply towards understanding higher temperature systems. Innovative new techniques are needed to overcome the limitations imposed by UHV conditions. Such a technique has been recently developed and presents new opportunities for studying liquid interfaces.<sup>91</sup>

## 5.2 Previous Work on Liquid Jets

The use of a liquid beam technique pioneered by Faubel et al.<sup>91-94</sup> allows for the direct study of a continually renewed liquid surface. This technique involves pumping a liquid through a micron sized aperture, creating a microjet of water that is fed into a vacuum chamber. The main chamber is equipped with traditional pumps along with a liquid nitrogen filled shroud and reservoir to trap the water as it evaporates. This cryopumping along with the small liquid jet diameter provides a background pressure low enough to ensure that the measurements of the desorbing species are free from gas phase collisions. Surface science analytical tools can be used to probe the liquid surface with the use of differential pumping to ensure a low pressure in the detection region. The renewable nature of the liquid jet ensures a clean surface. This technique provides a unique opportunity to gain insight into the liquid interface as well as solvation in liquids using sensitive probes such as laser ionization time of flight (TOF)<sup>95-98</sup>, photoelectron spectroscopy (PES)<sup>92, 93, 99, 100</sup>, and x-ray photoelectron spectroscopy (XPS)<sup>101-104</sup>.

Previous work by Faubel et al. measured the ultraviolet photoelectron spectra (UPS) spectra of water and alcohols, finding different orientations for methyl, ethyl, and benzyl alcohol at the liquid surface<sup>92</sup>. These results also showed a lowering of several ionization bands compared to the gas phase measurements due to the effect of the molecular relaxation energy. Measuring the velocity distribution of H<sub>2</sub>O molecules evaporating from a 5  $\mu$ m liquid water beam, it was shown that the water is supercooled with a temperature below 210 K<sup>91</sup>. Sobott et al. have used a liquid beam to investigate ionic clathrates and found ‘magic number clusters’ from alkali metal salt solutions<sup>97</sup>. X-

ray spectroscopy has also been used to investigate the liquid water microjets<sup>102-105</sup>. This work presented the first experimental measurement of the lengthening of the oxygen-oxygen distance in the surface water molecules as well as the weakening of the hydrogen bonding at the surface reflected in the weakened electronic perturbations of surface water molecules.

The solvation structure of species in water is a matter of great interest and has been studied using numerous techniques such as Fourier transform infrared spectroscopy (FT-IR)<sup>27, 87, 106-109</sup>, gas phase cluster studies<sup>110-114</sup>, secondary ion mass spectrometry time of flight mass spectrometry (SIMS-TOF)<sup>18, 22, 115</sup>, molecular dynamics (MD) simulations<sup>3, 12, 20, 29, 116-122</sup>, and near edge x-ray absorption fine structure spectroscopy (NEXAFS)<sup>24, 101, 123, 124</sup>. Recently, the valence band photoemission spectra of water<sup>100</sup> and aqueous alkali-metal halide solutions<sup>99</sup> have been measured using synchrotron radiation coupled with a liquid jet source. The valence band photoemission spectrum of water has been previously inaccessible due to the interference of the vapor usually associated with the liquid water sample. Coupling the liquid jet with the synchrotron radiation overcame this problem and enabled the first full valence band photoemission measurement in the liquid phase<sup>100</sup>. Similar to the solid phase of water compared to the gas phase, the liquid phase photoelectron spectra shows broadened peaks which are shifted about 1.5 eV to lower binding energies<sup>100</sup>. This shift is attributed to the polarization of the water molecules around an ionized water molecule and changes in the orbitals of the water molecules due to the hydrogen bonding network. Specifically, the authors note that the  $3a_1$  orbital is strongly affected by the hydrogen bonding and the different configurations of the water molecules and shows the strongest energy-level splitting. These measurements were

repeated with aqueous alkali-metal iodide salt solutions in an effort to investigate the structure of hydrated anions and cations<sup>99</sup>. The electron binding energies of the solvated ions were found to be considerably lower than those in the gas phase. The shift in the electron binding energy from gas phase to solvated ion was modeled using a simple dielectric cavity model and correlates with the solvent reorganization energy.

## 5.3 Experimental Setup

### 5.3.1 Liquid Jet

A schematic of a custom high vacuum liquid jet chamber is shown in Figure 5.1. A Shimadzu HPLC pump delivers the solution at a constant flow rate with a 5  $\mu\text{m}$  filter placed on the inlet to prevent contamination which could easily clog the small aperture. The pump supplies a constant flow rate of 0.15 mL/min, yielding a pressure typically between 0.1-0.3 MPa in the pumping line. The tip of the microjet is a platinum-iridium disk pressed into a larger stainless steel disk designed to compress against an O-ring on the end of the nozzle. The Pt-Ir disk is a commercially available cone shaped electron microscope aperture with a 10  $\mu\text{m}$  orifice. The stainless steel disc has a top-hat shape made to compress the aperture onto an O-ring by a Cajon fitting to form the nozzle of the jet.

One of the main challenges with this work is preventing the aperture from clogging. Small contaminants can easily clog the 10  $\mu\text{m}$  aperture, and freezing can also cause the jet to clog. As stated, a filter was placed on the pump inlet to prevent any

particles from being taken into the pumping system. The solutions were made with nanopure water and kept in covered containers to prevent particulates from entering the system. The use of salt solutions also presents the possibility of corrosion of the metal. To reduce this, dilute solutions were used with the most concentrated solution being  $10^{-1}$  M. The higher concentrations ( $\geq 10^{-2}$  M) were used for a minimal amount of time followed by a thorough flushing of the system.

A heater was also added to the system so the temperature of the nozzle could be controlled. The resistive heater was placed upstream of the nozzle. The nozzle temperature was most important while pulling vacuum, as this was the most common time for the jet to freeze and clog, and was held constant during the experiments.

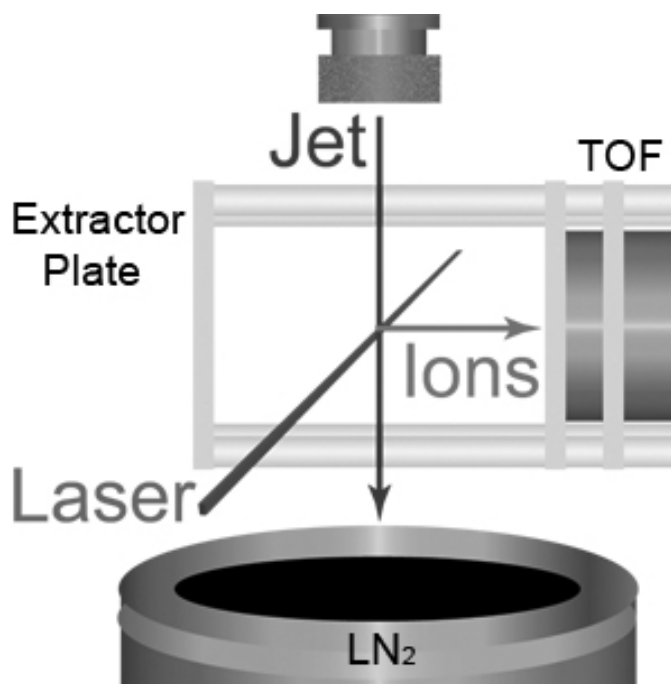


Figure 5.1 Schematic of liquid jet chamber

As shown in Figure 5.1, the liquid jet assembly is mounted vertically on an x-y-z translation stage in the center of the chamber. The jet is intersected by a focused laser beam. Movement in the x-y direction allows the jet to move in and out of the laser beam and maximize the signal intensity by aligning the jet in the center of the TOF. Movement in the z-direction allows us to sample different heights of the liquid jet, essentially measuring different temperatures and salt concentrations. A small cryotrap made of copper tubing with circulating liquid nitrogen above the liquid jet is used to trap evaporating water creating a nearly collision free evaporation process. About 10 cm below the liquid jet is the main pumping stage. A liquid nitrogen filled shroud and dewar traps the majority of the water vapor as it evaporates from the liquid jet and keeps the overall pressure in the chamber at or below  $10^{-5}$  torr. A turbomolecular pump is also used in conjunction with the cryotrap to maintain the vacuum. The TOF is differentially pumped with a separate turbomolecular pump to maintain  $10^{-6}$  torr pressure in the flight tube.

### 5.3.2 Excimer Laser

An argon fluoride excimer laser provides 193 nm UV light for photoionization of the liquid beam. The laser beam is focused on the liquid jet and operated at 10 Hz for maximum power. The power dependence of the spectra was taken using a beam attenuator placed in the path of the laser. The maximum laser power typically obtained was  $\sim 0.4$  mJ/pulse. The laser power varied with a shot to shot variation of  $\sim 20 - 50$   $\mu$ J/pulse. Attempts to reduce this shot to shot variation in power were made by replacing



the reflecting mirror in the laser and purging the gas vessel several times, but were unsuccessful. This large variation precluded the measurement of threshold values for cluster ion production however reproducible spectra were obtained and average values were used to construct the power dependences of the cluster ions.

### 5.3.2 Time-of-Flight (TOF) Mass Spectrometer

The TOF is mounted perpendicular to the jet and the laser beam and is differentially pumped with a turbomolecular pump. The ion optics protrude into the main chamber with the liquid jet flowing between the repeller and extractor plates of the TOF (Figure 5.1). The ions are accelerated through an Einzel lens and proceed through a flight tube  $\sim 1$  meter in length. The ions are detected by multichannel plates and the TOF spectra are recorded with a multichannel scaler, adding 5000 laser shots per spectra. It should be noted that the signal is not constant from shot to shot. When recording individual laser shots on an oscilloscope, there are shots where no ion signal is measured. Thus, the spectra recorded are an average ion signal produced from the laser ionization of the jet.

### 5.3.3 Salt Solutions

Sodium salts with anions of bromide, chloride, and iodide were used at concentrations ranging from  $10^{-4}$  M to  $10^{-1}$  M in steps of an order of magnitude. Special care was taken with NaI which is photosensitive. The NaI solution was made

immediately prior to use and kept in a covered bottle to prevent photochemical reactions from occurring in the solution. While changing solution concentrations, spectra were recorded until a stable signal was measured for at least three consecutive spectra.

## CHAPTER 6

### PHOTO-STIMULATED DESORPTION OF SODIUM SALT SOLUTIONS IN A LIQUID JET

#### 6.1 Overview

A liquid microjet was employed to examine the air/liquid interface of sodium salt solutions in the  $10^{-4}$  to  $10^{-1}$  M concentration range. Photoionization by a 193 nm excimer laser caused localized Coulomb explosions by repulsion of nearby charges, and the desorbing cations were detected with a time of flight mass spectrometer. Cluster ions of the form  $\text{H}^+(\text{H}_2\text{O})_n$  and  $\text{Na}^+(\text{H}_2\text{O})_m$  were detected. The protonated water cluster yield decreased with increasing salt concentration, while the solvated sodium ion cluster yield displayed the opposite trend. Power dependence studies indicate a multiple photon process, with the protonated water cluster ions requiring more photons than the solvated sodium ion clusters. At high concentrations,  $\text{Br}^+$  and  $\text{I}^+$  were seen in the cation desorption channel, however  $\text{Cl}^+$  was not observed. The cluster ion yield as a function of the number of water molecules can be modeled with a simple probability function involving the activation energy of the process as well as the available energy of the system. Deviations in the  $10^{-1}$  M solutions indicate a concentrated surface creating a highly ionic interface with a propensity of anions at the surface.

## 6.2 Time-of-Flight (TOF) Spectra

The cation yields resulting from 193 nm irradiation of NaCl salt solutions ranging in concentrations from  $10^{-4}$  M to  $10^{-1}$  M are shown in Figure 6.1. The mass scale was calibrated with several different salt solutions of varying cations ( $\text{Li}^+$ ,  $\text{Na}^+$  and  $\text{K}^+$ ). The TOF spectra of NaBr and NaI (not shown) are similar to that of the NaCl. The main cation products in the TOF spectra are  $\text{Na}^+$  (not shown),  $\text{H}^+(\text{H}_2\text{O})_n$ , and  $\text{Na}^+(\text{H}_2\text{O})_m$ . In the dilute solution (top spectra of Figure 6.1), only protonated water clusters are observed. With increasing concentration, the yield of solvated sodium ion clusters increases, dominating the spectra at  $10^{-1}$  M concentration (bottom spectra of Figure 6.1). At high concentrations ( $\geq 10^{-2}$  M) the  $\text{Na}^+$  peak saturates the detector resulting in a non-quantitative split-peak feature. The low mass section of the spectra is complicated with interference from scattered laser light and unresolved features, however in the mass range of the clusters, a near-zero baseline is measured.

## 6.3 Concentration Dependence of Cation Yield

The overall abundance of the protonated water clusters and the solvated sodium ion clusters is dependent on the concentration of the solution as shown in Figure 6.2. Figure 6.2 illustrates the change in the cluster ion yields as a function of concentrations for NaCl (top panel), NaBr, (middle panel), and NaI (bottom panel) with the protonated clusters shown as solid symbols, ( $\bullet$ )  $n=2$ , ( $\blacktriangledown$ )  $n=3$ , ( $\blacksquare$ )  $n=4$ , and solvated sodium ion clusters shown as open symbols, ( $\circ$ )  $m=1$ , ( $\nabla$ )  $m=2$ , ( $\square$ )  $m=3$ . In general the protonated

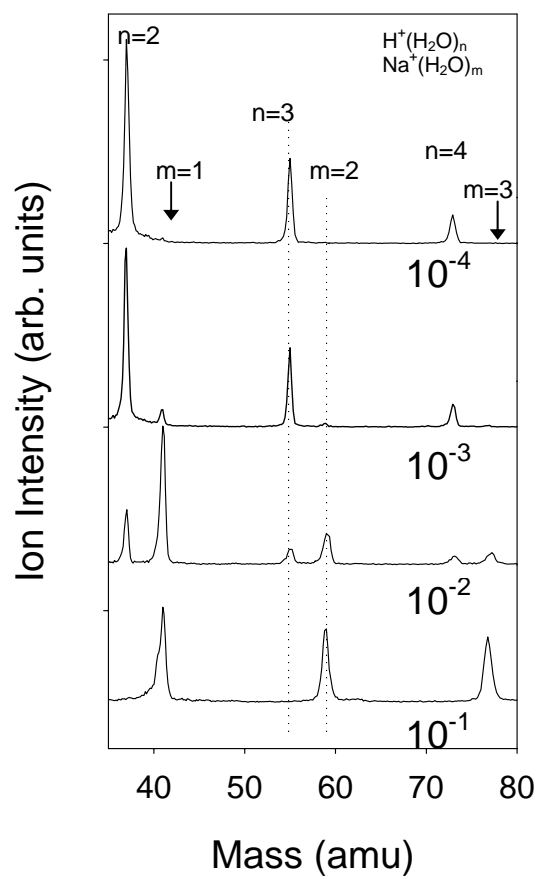


Figure 6.1 TOF spectra of sodium salt solutions of concentrations from  $10^{-4}$  –  $10^{-1}$  M

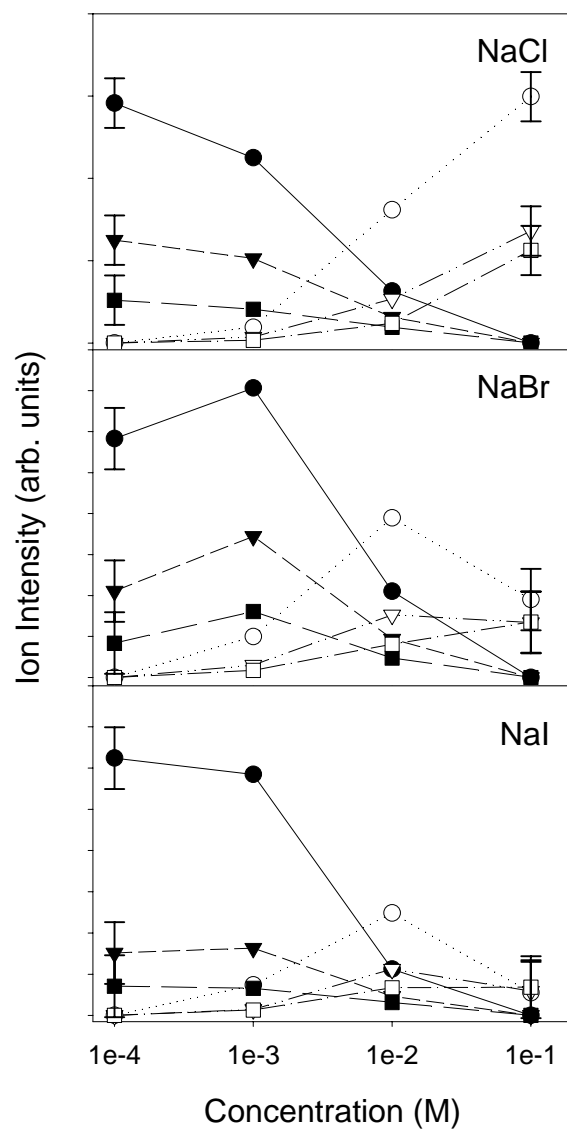


Figure 6.2 Concentration dependence of cluster yield from NaCl, NaBr and NaI

water cluster yields decrease with increasing salt concentration, while the solvated sodium ion clusters increase with concentration. At  $10^{-4}$  M, the protonated water cluster yields dominate the spectra. At this low concentration, no solvated sodium ions are observed. With  $10^{-3}$  M solution, protonated water clusters continue to dominate the spectra however they decrease in yield compared to the  $10^{-4}$  M solution. There is also a small yield of solvated sodium ion clusters that appear at  $10^{-3}$  M. Increasing the concentration to  $10^{-2}$  M results in a major change in the TOF spectra. The yield of solvated sodium ion clusters increases and is equal to or greater than the yield of protonated water clusters, which continue to decrease. Finally at  $10^{-1}$  M solution, there are no protonated water clusters and only solvated sodium ion clusters are present. A deviation in the general trend is observed for  $10^{-1}$  M NaBr and NaI solutions for  $m = 2$  and  $m = 3$ . There is a decrease in these cluster yields which is not observed with NaCl. It should be noted that the  $10^{-1}$  M NaBr and NaI solutions also have additional features due to desorption of the anion species that will be discussed in detail later in this chapter. This general trend of decreasing protonated water clusters and increasing solvated sodium ion clusters is observed with all of the salts used in this work.

#### **6.4 Anion Dependence of Cation Yield**

While only protonated water clusters and solvated sodium ion clusters are seen from NaCl solution, NaBr and NaI have additional desorption features. The TOF spectra of NaCl and NaBr from  $10^{-4}$  M to  $10^{-2}$  M are indistinguishable, displaying only protonated water clusters and solvated sodium ion clusters. At  $10^{-1}$  M concentration, the

NaBr solution has additional desorption features, as seen in Figure 6.3, corresponding to the mass of the anion.  $\text{Br}^+$  appears around mass 80 amu with two isotopes of approximately equal value (the stable isotopes of Br are 79 and 81 amu). This new peak has a width corresponding to roughly four mass units and is accompanied by a smaller peak  $\sim 18$  mass units higher, indicating a solvated species ( $\text{Br}^+(\text{H}_2\text{O})$ ). The intensity of the  $\text{Br}^+$  peak is on the order of the solvated sodium ion clusters.

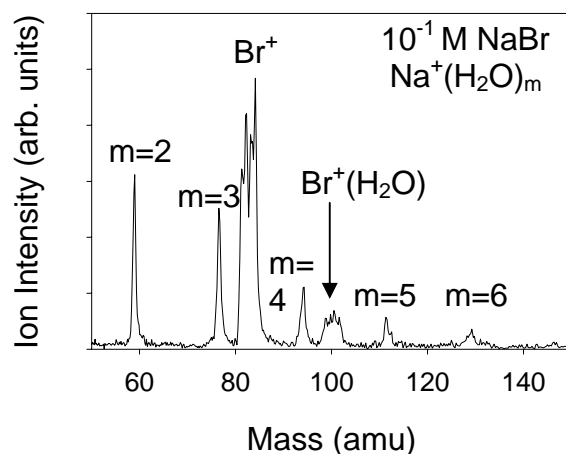


Figure 6.3 TOF spectra of  $10^{-1}$  M NaBr solution

The NaI solution also has a desorption feature corresponding to the mass of the anion. This feature is present at all concentrations, however a dramatic increase in its yield is observed at  $10^{-1}$  M. This increase is accompanied by additional peaks corresponding to solvated cluster ions which can be seen in Figure 6.4. The prominent  $\text{I}^+$  is observed with solvated species occurring at 18 amu intervals above the  $\text{I}^+$  peak. The enhancement of the peak  $\sim 253$   $m/z$  ratio is most likely  $\text{I}_2^+$  which is formed in concentrated NaI solutions.



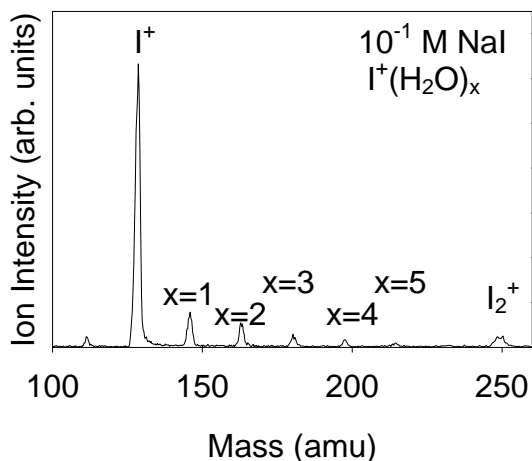


Figure 6.4 TOF spectra of  $10^{-1}$  M NaI solution

### 6.5 Flux Dependence of Cation Yield

The laser power was varied by placing a beam attenuator in the path of the laser to obtain a power dependence of the cluster ion yield. The maximum power of the laser was  $\sim 0.4$  mJ/pulse, with clusters detected as low as 0.1 mJ/pulse. Figure 6.5 shows the cluster yield as a function of laser power for  $10^{-2}$  M NaI, with protonated clusters shown as solid symbols, ( $\bullet$ )  $n=2$ , ( $\blacktriangledown$ )  $n=3$ , ( $\blacksquare$ )  $n=4$ , and solvated sodium ion clusters shown as open symbols, ( $\circ$ )  $m=1$ , ( $\nabla$ )  $m=2$ , ( $\square$ )  $m=3$ . Although the overall yield of the protonated water clusters and solvated sodium ion clusters changed with concentration, there was no change in the power dependence correlated with concentration within the range used in

this work. The data indicates a multiple photon process that is highly non-linear, with an average of 3-5 photons involved.

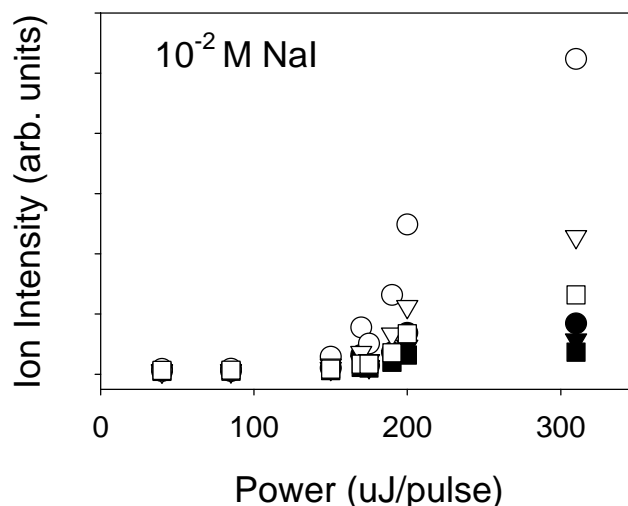


Figure 6.5 Power dependence of cation yield from a  $10^{-2}$  M NaI solution

## 6.6 Collision Free Desorption

The nearly collision free desorption and detection of the ions from the liquid interface is the unique nature of this technique. If we assume that the vapor pressure of the liquid determines the number density of the molecules immediately above the surface, the probability that a molecule undergoes a collision can be estimated by the mean free path of the molecule<sup>125</sup>. The mean free path can be calculated with the corresponding vapor pressure for water at the freezing point and is estimated to be  $\sim 15 \mu\text{m}$ . The Knudsen number, which compares the mean free path of a molecule with some characteristic length (in this case the diameter of the jet) is greater than 1. This value

provides insight into the collision probability and reveals that evaporating molecules are unlikely to experience any collisions upon evaporation from the jet. The likelihood of a collision further decreases with increasing distance from the jet because the density of molecules decreases with distance away from the liquid surface. This allows us to probe the liquid interface and measure the desorption products in the absence of gas phase interactions.

## 6.7 Evaporation from Jet Surface

The evaporation of the surface water molecules has two main effects on the jet. First, the desorbing water molecules cool the jet, and second, the concentration of the solute increases at the jet surface. A series of calculations by Faubel et al. investigated the temperature change due to the evaporation rate of the water molecules from the jet surface<sup>91</sup>. The evaporating molecules remove the heat of vaporization from the jet resulting in significant temperature changes that can occur on the  $10^{-8}$  second timescale<sup>91</sup>. The jet temperature was also investigated experimentally by measuring the velocity distribution of the evaporating water molecules. Under the assumption that the liquid jet surface is in equilibrium with the desorbing water molecules, the temperature was found to decrease by  $\sim 30$  K only 4 mm from the nozzle. The calculated and experimental temperatures for a jet of 5  $\mu\text{m}$  diameter differ by at least 30 K but show the same trend with increasing distance from the nozzle.

The evaporation of the water molecules from the jet surface is responsible for the concentration dependence measured between  $10^{-4}$  and  $10^{-1}$  M. In a  $10^{-1}$  M solution of

sodium salt, the ratio of water molecules to  $\text{Na}^+$  ions is 550:1. Given this ratio, it may seem puzzling that we would not produce any protonated water cluster ions. However, this scenario is explained by concentration of the  $\text{Na}^+$  at the jet surface due to the evaporation of the water molecules. The absence of protonated water cluster ions from a jet of  $10^{-1}$  M NaCl solution implies that all of the water molecules at the jet surface are found in the solvation shells of ions. As a first order approximation, we can use the change in the diameter of the jet calculated by the equations set forth by Faubel et al.<sup>91, 92</sup> to estimate the concentration of the jet surface. At a distance of 25 mm from the nozzle, the jet diameter decreases by  $\sim 0.3$  microns, corresponding to  $\sim 1000$  layers of water lost. If we assume that the sodium ions remained behind on the surface, this evaporation would leave two layers of sodium ions at the surface of the jet. This is obviously an upper limit estimation and does not account for diffusion or evaporation of a solvated sodium ion. This estimate illustrates that it is possible to have a large concentration of ions on the surface of the jet.

## **6.8 Mechanism and Model of Cation Desorption from the Liquid Jet Surface**

The mechanism of cation desorption from the liquid jet surface during pulsed UV laser excitation involves a Coulomb explosion resulting from the repulsion of charges on nearby molecules. The surface of the jet contains solvated ions, with the number of water molecules dependant on the concentration of the solution. Within the laser pulse, the water is ionized most likely by a non-resonant multiple photon process. The pre-existing  $\text{Na}^+$  ions near the newly created  $\text{H}_2\text{O}^+$  ions experience a Coulomb repulsion which is

proportional to the charges and the distance between the charges. If the two ions are within  $\sim 10 \text{ \AA}$  of each other, they are not effectively screened and can undergo a Coulomb explosion. The protonated water clusters are formed in a similar manner, however a water molecule must dissociate to transfer a proton to a neighboring water molecule. This can occur when a water molecule absorbs multiple photons, dissociating to form a trapped  $\text{H}_3\text{O}^+$ . The formation of the  $\text{H}_3\text{O}^+$  involves the rearrangement of bonds in neighboring water molecules, where the hydrogen bond between the molecules becomes a true bond, and the original O-H bond becomes a hydrogen bond. This  $\text{H}_3\text{O}^+$  ion will then undergo a Coulomb explosion induced by nearby sodium or water ions.

The distribution of the protonated water clusters and solvated sodium ion clusters with  $n$ ,  $m$  number of waters can be modeled by employing several factors including the enthalpy of solvation for the proton and sodium ions and the number of hydrogen bonds that must be broken to desorb a cluster with  $n$  water molecules. This model is similar to a model previously used for cluster desorption from ice surfaces with a few modifications. Figures 6.6 and 6.7 show the distribution of both protonated water clusters and solvated sodium ion clusters as a function of  $n$  ( $m$ ), the number of water molecules in the cluster for NaBr and NaCl solutions. The protonated water clusters are shown in Figures 6.6A and 6.7A for solutions ranging in concentrations from  $10^{-4} \text{ M}$  to  $10^{-2} \text{ M}$  (no protonated clusters are observed at  $10^{-1} \text{ M}$  concentration). Figures 6.6B and 6.7B show the solvated sodium ion cluster distribution from  $10^{-2} \text{ M}$  to  $10^{-1} \text{ M}$ . The data points represent the integrated area of the clusters while the model fit is shown as the lines in Figures 6.6 and 6.7, specifically ( $\triangle$ ) dotted line –  $10^{-4} \text{ M}$ , ( $\bullet$ ) solid line –  $10^{-3} \text{ M}$ , ( $\square$ ) dashed line –  $10^{-2} \text{ M}$ , ( $\blacklozenge$ ) dashed-dotted line –  $10^{-1} \text{ M}$ . The equation used to fit the data is

$$I(n) \sim \exp (-2 * E_H * n / E_n)$$

where  $E_H$  is the energy of a hydrogen bond (0.25 eV),  $n$  is the number of water molecules in the cluster, and  $E_n$  is the hydration enthalpy of the  $n^{\text{th}}$  water molecule in the cluster of size  $n$ <sup>79, 126</sup>. It is assumed that the interaction of the ion with the water molecule is an ion-dipole interaction, where the oxygen atoms of the water molecules are pointed toward the solvated cation. In this configuration, each water molecule must break two hydrogen bonds to desorb. The values of  $E_n$  were taken from measurements of Dalleska et al. obtained from collision-induced dissociation of water and sodium ion clusters<sup>79, 126</sup>. Only the first four sodium ion clusters could be modeled using this equation due to the limit of the sodium solvation enthalpy.

The  $m = 3$  cluster does not follow the exponential decrease in the trend for  $10^{-1}$  M solutions. The  $\text{Na}^+(\text{H}_2\text{O})_3$  yield is slightly larger than the  $\text{Na}^+(\text{H}_2\text{O})_2$  yield. This enhancement may reflect a pre-formed stable structure at the jet surface that occurs in concentrated solutions, resulting from a shared-solvation shell configuration with neighboring ions.

The bromide and iodide anions are most likely ionized during the laser pulse through a multiple photon process, as indicated by the power dependence. The positively charged iodine or bromine then feels the repulsive forces from the surrounding solvated sodium ions and can desorb in a Coulomb explosion. These positively charged halogen species can also form when the in the solution, since bromide will disproportionate and form HOBr in solution. Similar chemistry occurs for iodide. The formation of these complexes creates pre-formed positively charged halogen atoms in the jet solution. The

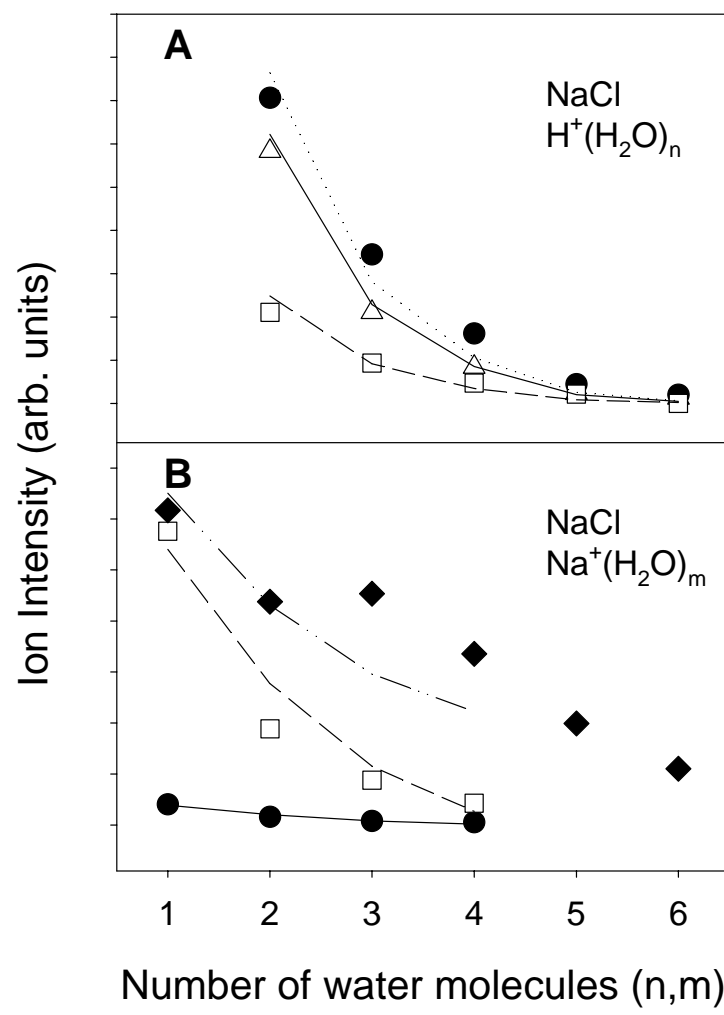


Figure 6.6 Model fit of cluster distribution from NaCl solutions

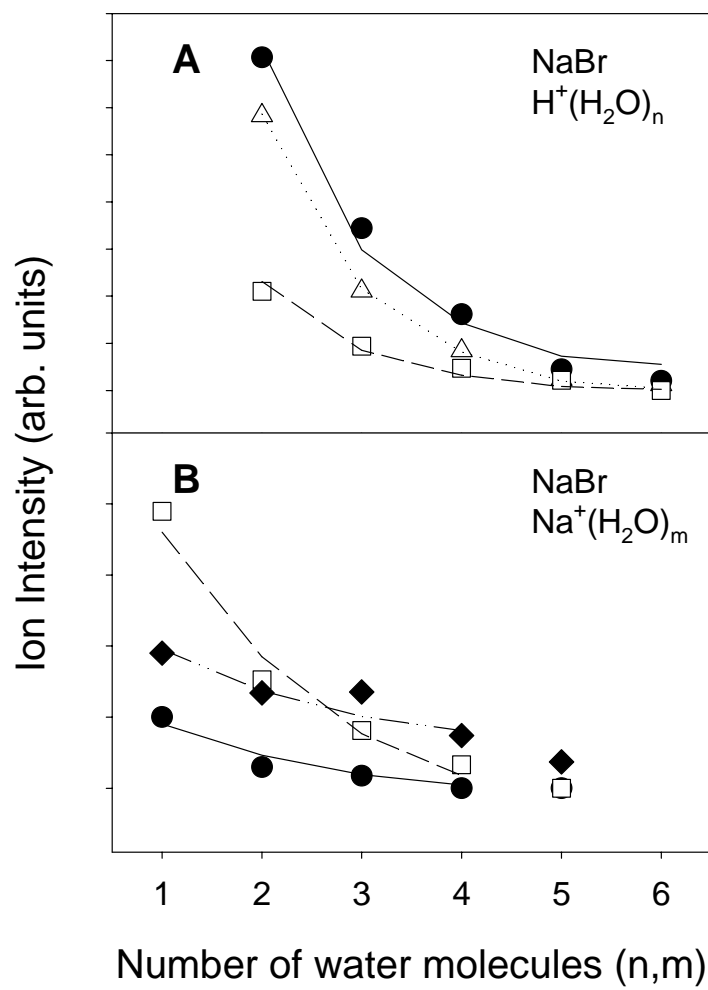


Figure 6.7 Model fit of cluster distribution from NaBr solutions



ionization of nearby water molecules can then cause a Coulomb explosion which ejects the  $\text{Br}^+$  or solvated  $\text{Br}^+(\text{H}_2\text{O})$  species. The likelihood of these desorption events increases with the probability of finding the species at the surface. Since the large polarizable species are more likely to be found at the surface, the iodide and bromide are therefore more likely to be seen in the cation desorption channel. No desorption features are seen corresponding to the mass of the anion or hydrated anion species in the TOF of NaCl solutions, most likely because the polarizability of this species is smaller than bromide and iodide so it is less likely to be found at the jet surface.

## **6.9 Analysis of Photon Flux Dependence**

The change in the ion yields as a function of the laser power was used to determine the number of photons involved in the ionization/desorption process over a flux range of  $\sim 0.05$  to  $\sim 0.35$  mJ/pulse. It was our goal to determine a precise photon dependence as this would provide valuable insight into the mechanism of the cluster ion production, however this was not possible due to the laser intensity variability. It is clear that a multiple photon process is involved and some general trends are observable. In general, the photon dependence, defined as the number of photons involved in a process, is higher for the protonated water clusters compared to the solvated sodium ion clusters. The protonated water clusters require 3 - 5 photons, while solvated sodium ions require 2 - 3 photons. The protonated water clusters require a greater number of photons because a  $\text{H}_3\text{O}^+$  ion must first be created, followed by repulsion from a nearby  $\text{Na}^+$  or  $\text{H}_2\text{O}^+$ . The photon dependence of the NaI solution was lower than that of the NaCl and NaBr

solutions, indicating that a one photon process may be possible. We also observed a general trend of a small decrease in the photon dependence with increasing number of water molecules in the cluster ion. This trend may reflect the change in the ratio of available water molecules to the ions created by the laser pulse. As the number of ions increases with the flux, there are fewer water molecules to solvate each charge, increasing the yield of clusters with 2 - 4 water molecules. This possible shift in the distribution of the yield with flux affects the photon dependence analysis, causing the smaller clusters to have a greater photon dependence than the larger clusters. The variance in the photon dependence may also be the result of different surfaces being present within the timescale of the laser pulse (2.5 nsec). During the initial period of the laser pulse, there may be a steep rise in the ion signal, however the number of desorbing clusters may decrease during the pulse because the surface of the jet has changed due to the initial desorption of ions. This would cause the yield to be smaller than expected and would be especially important for higher flux measurements which can dramatically change the surface of the jet in a short timescale.

## CHAPTER 7

### CONCLUSION

#### 7.1 Relevant Atmospheric Chemistry Studies

The traditional picture of reactions in aerosols mainly involved bulk processes that occurred through a multi-step process that involved diffusion of the gas to the aerosol surface, mass accommodation onto the particle, diffusion into the bulk and finally reaction<sup>127</sup>. When the kinetic rates for these processes were added to atmospheric models, the results were inconsistent with measurements. As early as 1990, it was proposed that unique surface species were involved in relevant processes in atmospheric chemistry<sup>128</sup>. Several subsequent studies supported this supposition<sup>129-131</sup>, although ATR-FT-IR failed to measure a surface specific species<sup>132</sup>. Investigations of the reactions involving  $\text{ClONO}_2$ ,  $\text{HCl}$ , and  $\text{H}_2\text{O}$  in sulfuric acid solutions by Hanson and Ravishankara<sup>133</sup> also suggested reactions at the surface played an important role in the chemistry of these species. Kinetic modeling of the system failed when the traditional uptake coefficient was used to fit the data, especially at high values of partial pressure of  $\text{HCl}$ . When a linear term was added to the kinetic model which assumed the uptake due to a surface reaction was proportional to the surface concentration of  $\text{HCl}$ , a better fit to the data was obtained. Together, these studies advanced the importance of heterogeneous chemistry in the kinetic models involving particles.

The production of  $\text{Cl}_2$  from surface reactions on particles was shown to be important in flow-tube studies by Hanson and Ravishankara<sup>134</sup>. An enhanced uptake of  $\text{ClONO}_2$  was measured for HCl doped nitric-acid trihydrate (NAT) surfaces, indicating a reaction between the species whose expected products are  $\text{HNO}_3$  and  $\text{Cl}_2$ . The reaction may proceed through a  $\text{HOCl}$  intermediate, as the authors investigated and found direct experimental observations of the reactions of HCl and  $\text{HOCl}$  to produce  $\text{Cl}_2$ . The authors conclude that  $\text{ClONO}_2$  reacts rapidly with HCl, either directly or through an  $\text{HOCl}$  intermediate species, forming  $\text{Cl}_2$  which desorbs from the surface on which the reaction occurs<sup>134</sup>. Since this reaction occurs on the surface of particles, the authors state that it is the identity of the surface which is important rather than the bulk concentration of species.

The reactivity of  $\text{ClONO}_2$  towards solvated chloride ions was also shown in cluster studies by Gilligan and Castleman<sup>135</sup>. No nitrate containing product ions were observed when protonated water clusters were exposed to  $\text{ClONO}_2$ , indicating that a heterogeneous reaction had not taken place. However, nitrate containing peaks were observed when the reactant clusters were doped with  $\text{DCl}$ . The presence of the chloride ion in the cluster provided an ionic interface which was more reactive towards the  $\text{ClONO}_2$ . These cluster experiments support an ionic solvation mechanism where the interfacial chloride ions play an important role in the heterogeneous reaction.

While the experimental work suggests surface specific reactions involved in several reaction pathways, investigating the nature of these surfaces and intermediates involved in the heterogeneous reactions presents challenges. As stated previously, the relevant pressures and temperatures at which these reactions occur preclude the use of

sensitive surface science techniques due to the vapor pressure, and traditional techniques lack the sensitivity to detect the surface species. While low-temperature ice studies do not reproduce the stratospheric conditions, we can start to gain insight into the interactions of adsorbates with water surfaces. After studying the well controlled low temperature ice system<sup>45</sup>, we extended the temperature range of our investigation by using a liquid microjet<sup>136</sup>. Within the past few years, there have been numerous exciting advances with regard to the understanding the air/liquid interface.

Molecular dynamics studies by Tobias and Jungwirth<sup>12-15</sup> have found that large polarizable anions are enhanced at the air/liquid interface of aqueous solutions. From an electrostatic perspective, the interface should be depleted of ions due to Born repulsion. However this is not the case when the forces due to the polarizability of the ions overcome this electrostatic repulsion. These calculations account for the polarizability of the bromide and iodide and show an enhancement at the interface. Smaller ions, such as sodium, are non-polarizable and fit into the hydrogen bonded water structure. Therefore, they can be easily solvated<sup>16</sup> unlike their anion counterparts. This view of ions at the interface presents added insight into the possible heterogeneous chemistry occurring on sea salt aerosols.

Recent collaborations have brought together experimental, molecular dynamics, and kinetics modeling studies investigating concentrated aqueous sodium chloride particles<sup>16</sup>. Experimental studies of photochemical reactions with ozone and concentrated NaCl particles monitored the production of Cl<sub>2</sub> with atmospheric pressure ionization-mass spectrometry (API-MS). Three initial ozone concentrations were used and the reactants and products were measured using differential optical absorption

spectroscopy and Fourier transform infrared spectroscopy (FT-IR)<sup>16</sup>. The kinetic model used for this system includes a number of gas phase species and reactions, as well as a number of aqueous phase species and reactions. This conventional model, called MAGIC (Model of Aerosol, Gas and Interfacial Chemistry) does not reproduce the observed Cl<sub>2</sub> production rate. Creating an acidified solution, which would specifically enhance the intermediate reaction of HOCl<sup>-</sup> + H<sup>+</sup> → H<sub>2</sub>O + Cl, predicts peak concentrations of Cl<sub>2</sub> that are much larger than experimentally observed. The traditional processes included in the kinetic model cannot reproduce the measurements from the aerosol chamber experiments. In light of the molecular dynamics studies, an interfacial reaction was proposed in which the chlorine ions at the air/liquid interface form a complex with an OH radical. A conservative approach was taken to estimate the reaction rate for formation of the OH...Cl<sup>-</sup> surface species based on the collision rate, disregarding the possibility of longer residence times for OH collisions. Including these surface specific reactions provided a much better fit to the experimentally observed Cl<sub>2</sub> production levels. The new kinetic model was significantly more accurate in predicting the level of Cl<sub>2</sub> production as well as replicating the time dependent profiles. This model also provided excellent agreement to the time-averaged Cl and OH measurements in remote boundary layer conditions typically measured in the Southern Ocean<sup>137, 138</sup>. Another interesting result of the theoretical investigations found an increased affinity of the Cl<sup>-</sup> for the OH radical, which would act to enhance this interfacial reaction rate.

These results are consistent with our investigations of the interaction of HCl with low temperature ice surfaces. ESD products must be produced in the terminal water layers to desorb from the surface<sup>32, 45</sup>. From our measurements of the cluster yield from

HCl doped ice surfaces, we can infer that the surface becomes disordered due to reorientation of the surface water molecules around the  $\text{Cl}^-$  ion<sup>45</sup>. If this  $\text{Cl}^-$  ion were to diffuse into the bulk, the surface water molecules could restore hydrogen bonding and order in the terminal ice layers. The disruption of the surface indicates that the  $\text{Cl}^-$  ion remains near the surface of the ice, ‘locking in’ the disorder it induces.

The PSD of salt solutions in the liquid microjet is also consistent with previous investigations into the surfaces of aqueous salt solutions<sup>136</sup>. Although this is a more complicated system, the general trend of anions available at the surface is observed for the  $10^{-1}$  M solutions. The temperature range of the liquid microjet is comparable to stratospheric conditions, making this an attractive technique for further investigations. The ability to use surface science probes with a liquid interface of temperatures in this range relevant to atmospheric processes provides a unique opportunity to gain insight into the surfaces involved in heterogeneous chemistry.

While there are numerous investigations into the interaction of HCl on ice and polar stratospheric cloud particles, there exist many conflicting results from the studies on this subject. One recent report of measured experimental isotherms of HCl on ice found the HCl surface coverage to be at least 100 times lower than the value currently used in modeling studies<sup>139</sup>. This measurement was taken with a careful analysis of the surface area of the ices prepared at temperatures relevant to the upper troposphere and lower stratosphere. The measured areas were much larger than the geometric area which had been used in numerous previous studies, affecting the determination of the HCl surface coverage. The authors employ a two-state model of adsorption with the adsorbed HCl forming a two-dimensional phase at the surface<sup>139</sup>. Although this study is at higher

temperature and pressure than our ESD measurements so we cannot directly compare results, our study is consistent with their conclusions. In the ESD studies, the HCl-dosed samples produce a high cluster yield typical of a disordered surface at very low HCl concentrations. This indicates that the HCl remains at the surface of the ice layer in our samples, supporting the proposed 2-D surface phase proposed by Henson et al<sup>139</sup>. This recent work on the isotherm measurements of HCl on ice highlights the need for further research into the nature of the heterogeneous chemistry and the applicability of laboratory measurements to modeling atmospheric conditions.

## **7.2 Implications of This Work to Atmospheric Chemistry**

The work presented in this thesis utilized surface sensitive techniques to examine interfaces relevant to atmospheric chemistry. The low temperature ice studies presented well-controlled surfaces with an opportunity to examine the hydrogen bonding network at the surface of the ice<sup>86</sup>. The ESD yields provided insight into the hydrogen bonding geometry of the terminal water layers because the excited states leading to desorption involve  $a_1$  bands, which are involved in hydrogen bonding. The protonated cluster ion yields exhibit the opposite phase dependence of the proton and  $H_2^+$  yields, decreasing from PASW to ASW to CI. The protonated water clusters are formed by a mechanism involving two-hole localization, hole transfer, and formation of a  $H_3O^+$ . Finally, a Coulomb explosion occurs from the repulsion of the charges leading to desorption of a cluster whose velocity is independent of mass. Threshold measurements show a small



yield  $\sim 25$  eV for  $\text{H}^+(\text{H}_2\text{O})$  with a distinct increase  $\sim 70$  eV, corresponding to two holes in the  $2a_1$  level.

This work was extended to also examine the interaction of  $\text{HCl}^{45}$ , an important species in the atmosphere relevant to ozone depletion, with the ice surface. By comparing the ESD yields of the pristine and  $\text{HCl}$  doped ice surfaces, we have found that  $\text{HCl}$  autoionizes at temperatures as low as 80 K and induces surface disorder in the terminal ice layers. This disorder increases the ESD cluster ion yields compared to pristine ice, a change which is most dramatic for crystalline ice samples.  $\text{HCl}$  also causes a decrease in the proton and  $\text{H}_2^+$  ESD yields, indicating that the dangling bonds are involved in the  $\text{HCl}$  adsorption and ionization.

The liquid microjet technique was used to measure the PSD of aqueous salt solutions<sup>136</sup>. Sodium salt solutions were chosen due to their importance in sea salt aerosol chemistry. A comparison of  $\text{NaCl}$ ,  $\text{NaBr}$ , and  $\text{NaI}$  solutions revealed an ion rich interface consistent with recent investigations of air/liquid interfaces<sup>12-14</sup>. Protonated water cluster ions and solvated sodium ions were measured from all of the salt solutions with intensities that depended on the concentration of the solution. Desorption features corresponding to the mass of the halogen and the solvated halogen cation were also seen in the positive ion channel for the  $10^{-1}$  M solutions of  $\text{NaBr}$  and  $\text{NaI}$ . Power dependence studies indicate a complex multiple photon process that is highly non-linear. The formation and desorption mechanism of the cluster ions results from the repulsion of two nearby ions. The protonated cluster ions require the formation of  $\text{H}_3\text{O}^+$ , which occurs by non-resonant multiple photon ionization of the water molecules. However, the solvated

sodium ion clusters are produced by the repulsion of the sodium ion and a nearby ionized water molecule at the jet surface.

### **7.3 Continuation of Research**

The next step to continue this work would be to examine the neutral species that desorb from these ice surfaces using resonance enhanced multiphoton ionization. Typically neutral desorption is a higher yield channel than cation desorption. Probing the specific states of the desorbed neutral species would provide further insight into the nature of the ice surface as well as the excited states produced at the ice surface. To add to the overall understanding of heterogeneous photochemical reactions on ice surfaces, PSD of the HCl-ice system in the wavelength region relevant to the actinic flux would be useful for probing possible products involving ionic interfaces. Specifically, the possibility of neutral halide desorption from the ice/liquid surface should be examined. As seen with the liquid jet experiments, the halide ions are easily ionized to neutral species due to their low electron affinities. The possibility of charge transfer to solvent states could create neutral species in photochemical reactions. These neutral halide species may not be tightly bound to the surface and desorb, adding an additional source term for these species.

While there still exists a gap between the temperature and pressure ranges in the stratosphere and the limits imposed by surface science techniques, useful information regarding interfaces pertinent to atmospheric chemistry can be obtained with traditional surface science tools. The relatively new liquid microjet technique may provide a

‘bridge’ between surface science and atmospheric chemistry that enables traditional surface science techniques to be applied to higher temperature interfaces of atmospheric relevance.

## 7.4 Conclusions

### 7.4.1 ESD of Pristine Ice Surfaces

Low-energy electron stimulated desorption has been used to study the production of  $\text{H}_2^+$  and protonated water clusters ( $\text{H}^+(\text{H}_2\text{O})_n$ ) from porous amorphous solid water (PASW), amorphous solid water (ASW), and crystalline (CI) water ice films. The data suggest that  $\text{H}_2^+$  production involves direct molecular elimination pathways from terminal water molecules and defect configurations and the surface. The latter involves intermolecular Coulomb interactions. The possibility of reactive scattering of an energetic proton cannot be ruled out with this data. Based upon the threshold measurements and kinetic energy distributions of the desorbing  $\text{H}_2^+$ , localized two-hole one-electron and/or two-hole final states containing  $3a_1$  and/or  $2a_1$  character are likely involved. The 70 eV cluster ion threshold implicates either a  $(2a_1^{-2})$  state localized on a monomer or the presence of neighboring water molecules; one with at least an initial  $2a_1^{-1}$  hole and the second with a hole in the inner valence region. This hole forms by either hole transfer, secondary electron scattering and/or energy exchange via correlation effects. The resulting correlated two-hole or two-hole, one-electron configurations are “localized” within a dimer (or larger) complex and result in an intermolecular Coulomb

repulsion and cluster ion ejection. Since the inner valence  $a_1$  levels are involved in hydrogen bonding and are perturbed via nearest neighbor coupling, the ESD cation yields are also extremely sensitive to the local potential and disorder in the terminal layer of the ice. This is consistent with the temperature dependent yield data and the valence band photoemission studies of ice as a function of temperature. The overall study clearly indicates the importance of intermolecular Coulomb interactions in weakly hydrogen bonded systems such as low-temperature water ice.

#### 7.4.2 Probing the Interaction of HCl with Ice Surfaces

The interaction and autoionization of HCl on ice was probed with low-energy electron stimulated desorption (ESD) and temperature programmed desorption (TPD). The ESD of  $H^+$ ,  $H_2^+$ , and  $H^+(H_2O)_{n=1-8}$  yields provided insight into the dynamic response of the terminal water molecules on an ice surface. Submonolayer concentrations of HCl produced a large reduction in the  $H^+$  and  $H_2^+$  signals as well as an increase in the protonated cluster yield ( $H^+(H_2O)_{n=1-8}$ ). These results are interpreted in terms of rapid ionization of HCl at the surface at temperatures as low as 80 K. The surface of the ice becomes disordered as HCl autoionizes and forms contact ion pairs, leading to reduced numbers of dangling bonds at the surface and increased hole localization. The decrease in the proton yield upon HCl dosing shows the importance of dangling bonds in HCl adsorption and ionization, in agreement with recent QM/MM calculations<sup>3, 30</sup>. The increase in the cluster yield with HCl results from the disorder present at the surface of the ice. The results are supported by TPD measurements with HCl desorption occurring

~ 150 K commensurate with bulk ice. TPD measurements show the presence of molecular HCl at dosing temperatures below 120 K however the dose required to adsorb molecular HCl is strongly dependent on the annealing history of the ice. At temperatures below those present in the stratosphere, the surface of the ice is a dynamic system and can solvate ions. Our results show the utility of ESD to probe low temperature ice surfaces.

#### 7.4.3 Photoionization of Sodium Salt Solutions in a Liquid Jet

The cation yields from the photoionization of a liquid jet of sodium salt solutions were examined as a function of concentration, laser power, and anion. The results indicate a multiple photon process which produces clusters desorbed by a Coulomb explosion. This localized desorption reveals the presence of a concentrated ionic interface. The cluster distribution can be modeled with a simple expression involving the energy required to break the hydrogen bonds of the water molecules and the enthalpy of the solvated cation, which changes with the number of water molecules in the cluster. This technique provides a unique opportunity to examine the air/liquid interface with surface sensitive probes such as photoionization.

## REFERENCES

1. Q. B. Lu and L. Sanche, *Phys. Rev. Lett.*, 87, 078501/1, (2001)
2. M. A. Zondlo, P. K. Hudson, A. J. Prenni and M. A. Tolbert, *Annu. Rev. Phys. Chem.*, 51, 473, (2000)
3. M. Svanberg, J. B. C. Pettersson and K. Bolton, *J. Phys. Chem. A*, 104, 5787, (2000)
4. M. J. Molina, T. L. Tso, L. T. Molina and F. C. Y. Wang, *Science*, 238, 1253, (1987)
5. R. E. Johnson, *Rev. Mod. Phys.*, 68, 305, (1996)
6. M. T. Sieger, W. C. Simpson and T. M. Orlando, *Nature*, 394, 554, (1998)
7. P. Wernet, D. Nordlund, U. Bergmann, M. Cavalleri, M. Odelius, H. Ogasawara, L. A. Naeslund, T. K. Hirsch, L. Ojamae, P. Glatzel, L. G. M. Pettersson and A. Nilsson, *Science*, 304, 995, (2004)
8. B. Boudaiffa, P. Cloutier, D. Hunting, M. A. Huels and L. Sanche, *Radiat. Res.*, 157, 227, (2002)
9. X. Pan, P. Cloutier, D. Hunting and L. Sanche, *Phys. Rev. Lett.*, 90, 208102/1, (2003)
10. A. B. Horn, J. R. Sodeau, T. B. Roddis and N. A. Williams, *J. Phys. Chem. A*, 102, 6107, (1998)
11. M. J. Molina, *Pure Appl. Chem.*, 68, 1749, (1996)
12. P. Jungwirth and D. J. Tobias, *J. Phys. Chem. B*, 104, 7702, (2000)
13. P. Jungwirth and D. J. Tobias, *J. Phys. Chem. B*, 105, 10468, (2001)
14. P. Jungwirth and D. J. Tobias, *J. Phys. Chem. B*, 106, 6361, (2002)
15. P. Jungwirth and D. J. Tobias, *J. Phys. Chem. A*, 106, 379, (2002)
16. E. M. Knipping, M. J. Lakin, K. L. Foster, P. Jungwirth, D. J. Tobias, R. B. Gerber, D. Dabdub and B. J. Finlayson-Pitts, *Science*, 288, 301, (2000)
17. D. R. Haynes, N. J. Tro and S. M. George, *Journal of Physical Chemistry*, 96, 8502, (1992)

18. H. Kang, T. H. Shin, S. C. Park, I. K. Kim and S. J. Han, *J. Am. Chem. Soc.*, 122, 9842, (2000)
19. P. U. Andersson, M. B. Ngrd and J. B. C. Pettersson, *J. Phys. Chem. B*, 104, 1596, (2000)
20. V. Buch, J. Sadlej, N. Aytemiz-Uras and J. P. Devlin, *J. Phys. Chem. A*, 106, 9374, (2002)
21. S. F. Banham, J. R. Sodeau, A. B. Horn, M. R. S. McCoustra and M. A. Chesters, *J. Vac. Sci. Technol., A*, 14, 1620, (1996)
22. H. A. Donsig and J. C. Vickerman, *J. Chem. Soc., Faraday Trans.*, 93, 2755, (1997)
23. L. Delzeit, B. Rowland and J. P. Devlin, *Journal of Physical Chemistry*, 97, 10312, (1993)
24. F. Bournel, C. Mangeney, M. Tronc, C. Laffon and P. Parent, *Phys. Rev. B*, 65, 201404/1, (2002)
25. J. Harnett, S. Haq and A. Hodgson, *Surface Science*, 532-535, 478, (2003)
26. J. D. Graham and J. T. Roberts, *Journal of Physical Chemistry*, 98, 5974, (1994)
27. S. Haq, J. Harnett and A. Hodgson, *J. Phys. Chem. B*, 106, 3950, (2002)
28. M. J. Isakson and G. O. Sitz, *J. Phys. Chem. A*, 103, 2044, (1999)
29. B. J. Gertner and J. T. Hynes, *Science*, 271, 1563, (1996)
30. K. Bolton, *Theochem*, 632, 145, (2003)
31. B. Boudaiffa, P. Cloutier, D. Hunting, M. A. Huels and L. Sanche, *Science*, 287, 1658, (2000)
32. M. T. Sieger, W. C. Simpson and T. M. Orlando, *Physical Review B: Condensed Matter*, 56, 4925, (1997)
33. T. M. Orlando and G. A. Kimmel, *Surface Science*, 390, 79, (1997)
34. G. A. Kimmel and T. M. Orlando, *Phys. Rev. Lett.*, 75, 2606, (1995)
35. G. A. Kimmel and T. M. Orlando, *Phys. Rev. Lett.*, 77, 3983, (1996)

36. W. C. Simpson, L. Parenteau, R. S. Smith, L. Sanche and T. M. Orlando, *Surface Science*, 390, 86, (1997)
37. R. A. Rosenberg, P. J. Love, P. R. LaRoe, V. Rehn and C. C. Parks, *Phys. Rev. B*, 31, 2634, (1985)
38. G. A. Kimmel, T. M. Orlando, P. Cloutier and L. Sanche, *J. Phys. Chem. B*, 101, 6301, (1997)
39. R. Souda, *Surface Science*, 511, 147, (2002)
40. M. T. Sieger and T. M. Orlando, *Surface Science*, 451, 97, (2000)
41. D. E. Ramaker, *Chemical Physics*, 80, 183, (1983)
42. R. A. Rosenberg, V. Rehn, V. O. Jones, A. K. Green, C. C. Parks, G. Loubriel and R. H. Stulen, *Chem. Phys. Lett.*, 80, 488, (1981)
43. R. Souda, *J. Chem. Phys.*, 117, 5967, (2002)
44. W. C. Simpson, M. T. Sieger, T. M. Orlando, L. Parenteau, K. Nagesha and L. Sanche, *J. Chem. Phys.*, 107, 8668, (1997)
45. J. Herring, A. Aleksandrov and T. M. Orlando, *Phys. Rev. Lett.*, 92, 187602/1, (2004)
46. T. M. Orlando, A. B. Aleksandrov and J. Herring, *J. Phys. Chem. B*, 107, 9370, (2003)
47. K. P. Stevenson, G. A. Kimmel, Z. Dohnalek, R. S. Smith and B. D. Kay, *Science*, 283, 1505, (1999)
48. R. J. Speedy, P. G. Debenedetti, R. S. Smith, C. Huang and B. D. Kay, *J. Chem. Phys.*, 105, 240, (1996)
49. R. S. Smith, C. Huang, E. K. L. Wong and B. D. Kay, *Surface Science*, 367, L13, (1996)
50. M. T. Sieger and T. M. Orlando, *Surface Science*, 390, 92, (1997)
51. R. S. Smith, C. Huang and B. D. Kay, *J. Phys. Chem. B*, 101, 6123, (1997)
52. W. C. Simpson, T. M. Orlando, L. Parenteau, K. Nagesha and L. Sanche, *J. Chem. Phys.*, 108, 5027, (1998)
53. J. O. Noell, C. F. Melius and R. H. Stulen, *Surface Science*, 157, 119, (1985)



54. M. A. Henderson, Surf. Sci. Rep., 46, 1, (2002)
55. P. A. Thiel and T. F. Madey, Surf. Sci. Rep., 7, 211, (1987)
56. E. Langenbach, A. Spitzer and H. Lueth, Surface Science, 147, 179, (1984)
57. M. Cavalleri, H. Ogasawara, L. G. M. Pettersson and A. Nilsson, Chem. Phys. Lett., 364, 363, (2002)
58. J. H. Guo, Y. Luo, A. Augustsson, J. E. Rubensson, C. Sathe, H. Agren, H. Siegbahn and J. Nordgren, 89, (2002)
59. G. Tzvetkov, Y. Zubavichus, G. Koller, T. Schmidt, C. Heske, E. Umbach, M. Grunze, M. G. Ramsey and F. P. Netzer, Surface Science, 543, 131, (2003)
60. K. Andersson, A. Nikitin, L. G. M. Pettersson, A. Nilsson and H. Ogasawara, Phys. Rev. Lett., 93, (2004)
61. T. M. Orlando and M. T. Sieger, Unpublished,
62. J. Appell and J. Durup, International Journal of Mass Spectrometry and Ion Physics, 10, 247, (1973)
63. H. H. Harris and J. J. Leventhal, J. Chem. Phys., 64, 3185, (1976)
64. H. C. Straub, B. G. Lindsay, K. A. Smith and R. F. Stebbings, J. Chem. Phys., 108, 109, (1998)
65. M. N. Piancastelli, A. Hempelmann, F. Heiser, O. Gessner, A. Rudel and U. Becker, Phys. Rev. A, 59, 300, (1999)
66. H. Rottke, C. Trump and W. Sandner, J. Phys. B, 31, 1083, (1998)
67. K. H. Tan, C. E. Brion, P. E. Van der Leeuw and M. J. Van der Wiel, Chemical Physics, 29, 299, (1978)
68. R. N. Barnett, H. P. Cheng, H. Hakkinen and U. Landman, Journal of Physical Chemistry, 99, 7731, (1995)
69. G. R. Floyd and R. H. Prince, Nature, Phys. Sci., 240, 11, (1972)
70. R. H. Prince and G. R. Floyd, Chem. Phys. Lett., 43, 326, (1976)
71. S. R. Baggott, K. W. Kolasinski, L. M. A. Perdigo, D. Riedel, Q. Guo and R. E. Palmer, J. Chem. Phys., 117, 6667, (2002)

72. R. Souda, Surface Science, 506, L275, (2002)
73. R. Souda, Phys. Rev. B, 65, 245419/1, (2002)
74. J. Bernholc and J. C. Phillips, J. Chem. Phys., 85, 3258, (1986)
75. L. S. Cederbaum, J. Zobeley and F. Tarantelli, Phys. Rev. Lett., 79, 4778, (1997)
76. H. Siegbahn, L. Asplund and P. Kelfve, 35, 330, (1975)
77. P. P. Radi, P. Beaud, D. Franzke, H. M. Frey, T. Gerber, B. Mischler and A. P. Tzannis, J. Chem. Phys., 111, 512, (1999)
78. B. Brena, D. Nordlund, M. Odelius, H. Ogasawara, A. Nilsson and L. G. M. Pettersson, Phys. Rev. Lett., 93, 148302/1, (2004)
79. N. F. Dalleska, K. Honma and P. B. Armentrout, J. Am. Chem. Soc., 115, 12125, (1993)
80. A. R. Burns, D. R. Jennison and E. B. Stechel, J. Vac. Sci. Technol., A, 5, 671, (1987)
81. M. Fisher and J. P. Devlin, Journal of Physical Chemistry, 99, 11584, (1995)
82. M. Akbulut, T. E. Madey and P. Nordlander, J. Chem. Phys., 106, 2801, (1997)
83. J. Herring-Captain, A. Aleksandrov and T. M. Orlando, Physical Review B: Condensed Matter, (2004, submitted)
84. J. D. Graham and J. T. Roberts, Geophys. Res. Lett., 22, 251, (1995)
85. V. Sadtchenko, C. F. Giese and W. R. Gentry, J. Phys. Chem. B, 104, 9421, (2000)
86. J. Herring-Captain, A. Alexandrov, G. Grieves, M. T. Sieger, H. Chen and T. M. Orlando, Phys. Rev. B, submitted, (2005)
87. J. D. Graham and J. T. Roberts, Chemometrics and Intelligent Laboratory Systems, 37, 139, (1997)
88. J. Harnett, S. Haq and A. Hodgson, J. Phys. Chem. A, 106, 9226, (2002)
89. W. Kuch, W. Schnurnberger, M. Schulze and K. Bolwin, J. Chem. Phys., 101, 1687, (1994)
90. J. W. He and P. R. Norton, Surface Science, 238, 95, (1990)

91. M. Faubel, S. Schlemmer and J. P. Toennies, *Z. Phys. D-Atoms Mol. Clusters*, 10, 269, (1988)
92. M. Faubel, B. Steiner and J. P. Toennies, *J. Chem. Phys.*, 106, 9013, (1997)
93. M. Faubel, B. Steiner and J. P. Toennies, *J. Electron Spectrosc. Relat. Phenom.*, 95, 159, (1998)
94. M. Faubel and B. Steiner, *Ber. Bunsen-Ges. Phys. Chem. Chem. Phys.*, 96, 1167, (1992)
95. F. Sobott, A. Wattenberg, W. Kleinekofort, A. Pfenninger and B. Brutschy, *Fresenius J. Anal. Chem.*, 360, 745, (1998)
96. A. Wattenberg, F. Sobott, H. D. Barth and B. Brutschy, *Eur. Mass Spectrom.*, 5, 71, (1999)
97. F. Sobott, A. Wattenberg, H. D. Barth and B. Brutschy, *Int. J. Mass Spectrom.*, 187, 271, (1999)
98. F. Sobott, W. Kleinekofort and B. Brutschy, *Analytical Chemistry*, 69, 3587, (1997)
99. R. Weber, B. Winter, P. M. Schmidt, W. Widdra, I. V. Hertel, M. Dittmar and M. Faubel, *J. Phys. Chem. B*, 108, 4729, (2004)
100. B. Winter, R. Weber, W. Widdra, M. Dittmar, M. Faubel and I. V. Hertel, *J. Phys. Chem. A*, 108, 2625, (2004)
101. K. R. Wilson, M. Cavalleri, B. S. Rude, R. D. Schaller, A. Nilsson, L. G. M. Pettersson, N. Goldman, T. Catalano, J. D. Bozek and R. J. Saykally, *J. Phys.: Condens. Matter*, 14, L221, (2002)
102. K. R. Wilson, B. S. Rude, T. Catalano, R. D. Schaller, J. G. Tobin, D. T. Co and R. J. Saykally, 105, 3346, (2001)
103. K. R. Wilson, B. S. Rude, J. Smith, C. Cappa, D. T. Co, R. D. Schaller, M. Larsson, T. Catalano and R. J. Saykally, 75, 725, (2004)
104. J. D. Smith, C. D. Cappa, K. R. Wilson, B. M. Messer, R. C. Cohen and R. J. Saykally, 306, 851, (2004)
105. K. R. Wilson, R. D. Schaller, D. T. Co, R. J. Saykally, B. S. Rude, T. Catalano and J. D. Bozek, 117, 7738, (2002)

106. B. G. Koehler, L. S. McNeill, A. M. Middlebrook and M. A. Tolbert, *J. Geophys. Res.*, [Atmos.], 98, 10, (1993)
107. S. B. Barone, M. A. Zondlo and M. A. Tolbert, *J. Phys. Chem. A*, 103, 9717, (1999)
108. J. E. Schaff and J. T. Roberts, *Langmuir*, 14, 1478, (1998)
109. J. R. Sodeau, A. B. Horn, S. F. Banham and T. G. Koch, *Journal of Physical Chemistry*, 99, 6258, (1995)
110. J. J. Breen, K. Kilgore, K. Stephan, R. Hofmann-Sievert, B. D. Kay, R. G. Keese, T. D. Mark and A. W. Castleman, Jr., *Chemical Physics*, 91, 305, (1984)
111. V. Hermann, B. D. Kay and A. W. Castleman, Jr., *Chemical Physics*, 72, 185, (1982)
112. A. J. Huneycutt, R. J. Stickland, F. Hellberg and R. J. Saykally, *J. Chem. Phys.*, 118, 1221, (2003)
113. R. S. MacTaylor and A. W. Castleman, Jr., *Journal of Atmospheric Chemistry*, 36, 23, (2000)
114. D. M. Upadhyay, M. K. Shukla and P. C. Mishra, *Int. J. Quantum Chem.*, 81, 90, (2001)
115. R. Souda, *J. Chem. Phys.*, 119, 2774, (2003)
116. R. Buesnel, I. H. Hillier and A. J. Masters, *Chem. Phys. Lett.*, 247, 391, (1995)
117. A. V. Egorov, E. N. Brodskaya and A. Laaksonen, *J. Chem. Phys.*, 118, 6380, (2003)
118. B. J. Gertner and J. T. Hynes, *Faraday Discussions*, 110, 301, (1998)
119. Y. A. Mantz, F. M. Geiger, L. T. Molina, M. J. Molina and B. L. Trout, *Chem. Phys. Lett.*, 348, 285, (2001)
120. D. J. Tobias, P. Jungwirth and M. Parrinello, *J. Chem. Phys.*, 114, 7036, (2001)
121. C. Toubin, S. Picaud, P. N. M. Hoang, C. Girardet, B. Demirdjian, D. Ferry and J. Suzanne, *J. Chem. Phys.*, 116, 5150, (2002)
122. C. Toubin, S. Picaud, P. N. M. Hoang, C. Girardet, R. M. Lynden-Bell and J. T. Hynes, *J. Chem. Phys.*, 118, 9814, (2003)

123. F. Bournel, C. Mangeney, M. Tronc, C. Laffon and P. Parent, *Surface Science*, 528, 224, (2003)
124. P. Parent, C. Laffon, C. Mangeney, F. Bournel and M. Tronc, *J. Chem. Phys.*, 117, 10842, (2002)
125. T. Kondow and F. Mafune, *Annu. Rev. Phys. Chem.*, 51, 731, (2000)
126. N. F. Dalleska, B. L. Tjelta and P. B. Armentrout, *J. Am. Chem. Soc.*, 98, 4191, (1994)
127. B. J. Finlayson-Pitts, *Chemical Reviews*, 103, 4801, (2003)
128. J. T. Jayne, P. Davidovits, D. R. Worsnop, M. S. Zahniser and C. E. Kolb, *Journal of Physical Chemistry*, 94, 6041, (1990)
129. S. M. Clegg and J. P. D. Abbatt, *Atmospheric Chemical Physics*, 1, 73, (2001)
130. J. Boniface, Q. Shi, Y. Q. Li, J. L. Cheung, O. V. Rattigan, P. Davidovits, D. R. Worsnop, J. T. Jayne and C. E. Kolb, *J. Phys. Chem. A*, 104, 7502, (2000)
131. D. J. Donaldson, J. A. Guest and M. C. Goh, *Journal of Physical Chemistry*, 99, 9313, (1995)
132. H. S. Yang, N. J. Wright, A. M. Gagnon, R. B. Gerber and B. J. Finlayson-Pitts, *Physical Chemistry Chemical Physics*, 4, 1832, (2002)
133. D. R. Hanson and A. R. Ravishankara, 98, 5728, (1994)
134. D. R. Hanson and A. R. Ravishankara, *Journal of Physical Chemistry*, 96, 2682, (1992)
135. J. J. Gilligan and A. W. Castleman, Jr., *J. Phys. Chem. A*, 105, 1028, (2001)
136. J. Herring-Captain, N. Petrick, A. Aleksandrov, R. Tonkyn, G. Kimmel and T. Orlando, *J. Phys. Chem. B*, in prep., (2005)
137. O. W. Wingenter, M. K. Kubo, N. J. Blake, T. W. Smith, D. R. Blake and F. S. Rowland, *J. Geophys. Res.*, [Atmos.], 101, 4331, (1996)
138. F. B. Griffiths, T. S. Bates, P. K. Quinn, L. A. Clementson and J. S. Parslow, *J. Geophys. Res.*, [Atmos.], 104, 21649, (1999)
139. B. F. Henson, K. R. Wilson, J. M. Robinson, C. A. Noble, J. L. Casson and D. R. Worsnop, *J. Chem. Phys.*, 121, 8486, (2004)